RESIDUAL SERVICE LIFE PROGNOSTIC MODELS FOR TAPERED ROLLER BEARINGS

A Thesis

by

JENNIFER DANNI LIMA

Submitted to the Graduate College of
The University of Texas Rio Grande Valley
In partial fulfillment of the requirements for the degree of

MASTER OF SCIENCE IN ENGINEERING

May 2020

Major Subject: Mechanical Engineering

RESIDUAL SERVICE LIFE PROGNOSTIC MODELS FOR TAPERED ROLLER BEARINGS

A Thesis
by
JENNIFER DANNI LIMA

COMMITTEE MEMBERS

Dr. Constantine Tarawneh
Chair of Committee

Dr. Arturo Fuentes
Committee Member

Dr. Robert Jones
Committee Member

May 2020

Copyright © 2019Jennifer Danni Lima

All Rights Reserved

ABSTRACT

Lima, Jennifer D., Residual Service Life Prognostic Models for Tapered Roller Bearings. Master of Science (MS), May 2020, 87 pp., 12 tables, 42 figures, 22 references.

There are a few different bearing health monitoring technologies currently used in the railroad industry, both reactive and preventative detection systems. Reactive models have proven to be ineffective in monitoring bearing health, which has resulted in either unnecessary train stoppages and delays or in-service failures and bearing burn-off leading to catastrophic train derailments. Wayside preventative detection systems, while more effective than reactive technologies, are scarce and neglect railcars' that do not travel over a specific route. This knowledge prompted the University Transportation Center for Railway Safety at UTRGV to develop an onboard bearing health monitoring system that can accurately assess the health of a bearing and identify the defective component at an early stage of the defect development. This system has been proven to accurately detect defective bearings through extensive laboratory testing validated by field testing performed at the Transportation Technology Center, Inc. in Pueblo, CO. Using this system, a prognostic model for the residual service life of a defective bearing was developed. This model can be used by the railroads to schedule proactive maintenance cycles to mitigate inefficient faulty bearing replacements.

DEDICATION

This thesis is dedicated to my family. To my father, who sparked in me a love for engineering. My older sister, Rossy, who always set a great example to follow. And my mother, Yolanda, for never giving up on me. I owe all my achievements to your love and support.

ACKNOWLEDGEMENTS

I don’t think I’m capable of expressing how grateful I am for my research director and mentor, Dr. Constantine Tarawneh. The dedication and tenacity that you show in all your endeavors is inspirational. You have provided me with so many things to be thankful for. You’ve helped me grow as a person and it is through your guidance that I have been able to accomplish so much. I found a second family at the University Transportation Center for Railway Safety. Thank you for believing me capable of obtaining my master’s degree and thank you for making a job feel like home.

I’d like to thank everybody from the UTCRS team. You guys are the best example of teamwork I’ve had the pleasure of seeing. I will always remember this time fondly and I know that all of you have a great future ahead.

I’d also like to show my appreciation for Dr. Fuentes and Dr. Jones, for their time and encouraging dispositions throughout the pursue of my Master’s degree. This could not have been accomplished without your aid. You are great professors and it is an honor to have been taught by you.

Finally, this study was made possible by funding provided by The University Transportation Center for Railway Safety (UTCRS), through a USDOT Grant No. #DTRT 13-G-UTC59.

DISCLAIMER

The contents of this thesis reflect the views of the authors, who are responsible for the facts and the accuracy of the information presented herein. This document is disseminated under the sponsorship of the U.S. Department of Transportation’s University Transportation Centers Program, in the interest of information exchange. The U.S. Government assumes no liability for the contents or use thereof.

TABLE OF CONTENTS

Page

ABSTRACT iii

DEDICATION iv

ACKNOWLEDGEMENTS v

DISCLAIMER vi

TABLE OF CONTENTS vii

LIST OF TABLES x

LIST OF FIGURES xi

CHAPTER I 1

- 1.1 Introduction 1
  - 1.1.1 Tapered Roller Bearings 1
  - 1.1.2 Railway Safety 4
- 1.2 Derailments and In-Service Failures 5
- 1.3 Wayside Condition Monitoring Systems 5
  - 1.3.1 Trackside Acoustic Detection System (TADS™) 6
  - 1.3.2 RailBAM® 6
  - 1.3.3 Hot-Box Detector (HBD) 7
- 1.4 Onboard Condition Monitoring Systems 8
  - 1.4.1 SMART-BOLT™ 9

1.4.2 Wireless Sensor Node 10
1.4.3 Timken Guardian™ Bearing 10
1.5 Purpose 11
CHAPTER II 13
2.1 Bearing Assembly 13
2.1.1 Measurements 14
2.1.2 Lubrication 15
2.2 Four-Bearing Tester (4BT) 16
2.3 Single-Bearing Tester (SBT) 19
2.4 Data Acquisition 21
CHAPTER III 22
3.1 Defect Detection 23
3.2 Spall Casting 27
3.3 Spall Growth Patterns 28
3.3.1 Inner Ring (Cone) 29
3.3.2 Outer Ring (Cup) 31
CHAPTER IV 34
4.1 RMS and Defect Area Correlation Models 34
4.2 Spall Growth Rate Patterns 39
4.3 Laboratory Experiment 43
4.3.1 Laboratory Experiment 200: Cup Defect 43

4.3.2 Laboratory Experiment 184B: Cup Defect 46

4.3.3 Laboratory Experiment 202A: Cone Defect 49

4.3.4 Laboratory Experiment 206: Cone Defect 52

CHAPTER V 57

REFERENCES 60

BIOGRAPHICAL SKETCH 62

LIST OF TABLES

Page

Table 1. Bearing dimensions and loading conditions 2

Table 2. Lubrication (grease)application measurements for class K and class F bearings........... 15

Table 3. Axle to Track Speed Conversions 16

Table 4. Catalogued condition parameters using RMS values 37

Table 5. Average values for the final two hours of Experiment 200 45

Table 6. Spall size and spall growth rate values for Experiment 200 45

Table 7. Average values for the final two hours of Experiment 184B 48

Table 8. Spall size and spall growth rate values for Experiment 184B 48

Table 9. Average values for the final two hours of Experiment 202A 51

Table 10. Spall size and spall growth rate values for Experiment 202A 51

Table 11. Average values for the final two hours of Experiment 206 55

Table 12. Spall size and spall growth rate values for Experiment 206 55

LIST OF FIGURES

Page

Figure 1. Components of a tapered roller bearing 1

Figure 2. Schematic showing direction of rotation relative to loaded and unloaded zones............ 3

Figure 3. Example of localized defects (left) and distributed defect (right).................................. 4

Figure 4. Photograph of a TADS™ site[6].. 6

Figure 5. Photograph of a RailBAM® system.. 7

Figure 6. Example of a Hot-Box-Detector (HBD) site[8] 8

Figure 7. Field installation of a Wireless Sensor Node 10

Figure 8. Cage measurement set-up: cage lift (left), cage shake (right)...................................... 14

Figure 9. Four-Bearing Tester (4BT).. 17

Figure 10. Modified 4BT adapter showing vibration sensors (left) and temperature sensors (right)... 18

Figure 11. Top view of four-bearing tester (4BT) 19

Figure 12. Single bearing tester (SBT) 20

Figure 13. Single bearing tester thermocouple locations: bayonets represented by black dots,K-type thermocouples represented by red dots 21

Figure 14. Defect detection algorithm flowchart [16] 24

Figure 15. RMS - Cup defect size correlation at 137 km/h (85 mph) and full load[16].............. 26

Figure 16. RMS - Cone defect size correlation at 137 km/h (85 mph) and full load[16]............. 26

Figure 17. Casting procedure using sealant and bismuth tape... 27

Figure 18. Spall regions depicted in inner rings: edge (left), center (center), full-width (right) 29
Figure 19. Cone spall size vs total distance traveled [20]........ 30
Figure 20. Cup spall size vs distance traveled [20] 32
Figure 21. Contact area models: convex inner ring (left), concave outer ring (right) 33
Figure 22. Improved regression analysis of RMS vs cup spall area 35
Figure 23. Improved regression analysis of RMS vs cone spall area 36
Figure 24. RMS vs cup spall area regression model with condition parameters 38
Figure 25.RMS vs cone spall area regression model with condition parameters 39
Figure 26. Cup spall area growth rate versus cup spall area 40
Figure 27. Cone spall area growth rate versus cone spall area 40
Figure 28. Cup spall area growth rate versus RMS 42
Figure 29. Cone spall area growth rate versus RMS 42
Figure 30. Experiment 200: Initial cup raceway (left) and final cup raceway (right) 43
Figure 31. Vibration and temperature profiles for Experiment 200 44
Figure 32. Experiment 200 cup spall growth rate in relation to the developed regression model 45
Figure 33. Experiment 184B: Initial cup raceway (left) and final cup raceway (right) 47
Figure 34. Vibration and temperature profiles for Experiment 184B 47
Figure 35. Experiment 184B cup spall growth rate in relation to the developed regression model 48
Figure 36. Experiment 202A: Initial cone raceway (left) and final cone raceway (right) 49
Figure 37. Vibration and temperature profiles for Experiment 202A 50

Figure 38. Experiment 202A cone spall growth rate in relation to the developed regression model 51
Figure 39. Experiment 206 initial cone raceway (multiple spalls) 53
Figure 40. Experiment 206 final cone raceway 53
Figure 41. Vibration and temperature profiles for Experiment 206 54
Figure 42. Experiment 206 cone spall growth rate in relation to the developed regression model 55

CHAPTER I

BACKGROUND & INTRODUCTION

1.1 Introduction

1.1.1 Tapered Roller Bearings

A typical freight car can weigh between 30 to 130 tons, depending on loading conditions. These loads are supported by various suspension components such as springs, dampers, wheels, axles, and tapered roller bearings. Railcars are equipped with two frontal and two rear wheel-axle assemblies, allowing for a total of eight tapered roller bearings per car. A single tapered roller bearing can sustain 16 ton loads and will undergo speeds of up to 129 km/h (80 mph).Due to the high travel velocities and heavy cargo loads experienced, bearing failure is in the top three leading causes for derailments [1].

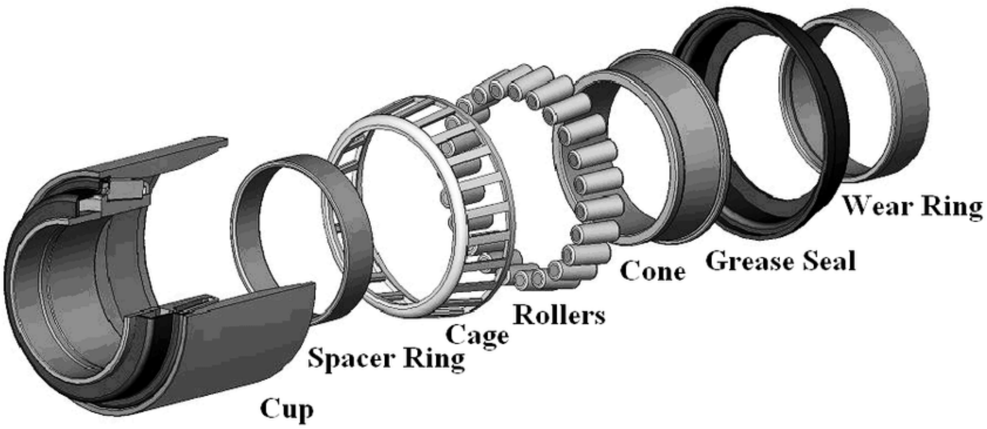

Figure 1. Components of a tapered roller bearing

The three primary components in a tapered roller bearing are the outer ring (cup), inner ring (cone) and rollers. The outer ring houses two inner rings. Each inner ring is surrounded by

23 rollers which are held together against the inner ring by a cage. Separating the cones is a spacer ring which varies in size depending on the bearing cup class. The Association of American Railroads (AAR) classifies bearings according to their size and load carrying capacity. The two principle bearing classes studied are class K and class F, their dimensions and loading conditions can be observed in Table 1, along with a few other common bearing classes. Seeing that Class F and Class K bearings share the same cup diameter they have identical nominal bearing loads and can use the same inner ring type.

Table 1. Bearing dimensions and loading conditions

Bearing Class	**Cup Dimension Diameter × Width [inch]**	**Bearing Load [kN] / [kips]**
E	6 × 11	117.0/26.3
F	6 ½ × 12	153.0/34.4
G	7 × 12	169.0/38.0
K	6 ½ × 9	153.0/34.4

The bearing outer ring (cup) is held stationary by the railcar load applied through the side frame. This creates a top loaded scenario as the one depicted in Figure 2. With the cup as a static element, it will experience constant forces as the movement-restricting loads are placed upon it. The cones, however, are able to rotate freely inside the cup, prompting this component to cycle in and out of the loaded zone. This cyclic loading results in the cone seeing smaller stresses and consequently less wear than that observed in the bearing cup. The rollers both rotate and revolve around the cone and thus see the least stress. These motions and varying load behaviors lead to the components having different spalling rates and defect development probabilities.

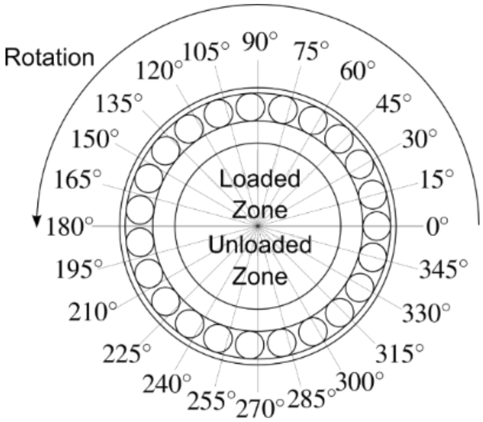

Figure 2. Schematic showing direction of rotation relative to loaded and unloaded zones

Bearing defects are categorized into three principle classifications: geometric, distributed, and localized. Geometric defects are caused by intolerances in the bearing geometry due to manufacturing errors. These defects are prone to causing high operation temperatures in a bearing without any visible signs of a surface flaw. A bearing is considered to have a distributed defect when a component has multiple imperfections along a raceway or when several components of the same bearing have developed a defect. An example of a distributed defect is shown in the water-etch inner ring in Figure 3 (right). Water-etch defects are caused by moisture entering the bearing, likely due to faulty seals. Once water enters, it commences a process of grease degradation which compromises the frictionless rotation common to a bearing and causes a sped abrasion rate in the components. Localized defects can be subcategorized into cracks, pits and spalls. Examples of spalling and pitting can be seen in Figure 3 (left).

Localized defects are primarily developed through the constant high stresses placed on subsurface inclusions of a steel component. Subsurface inclusions are caused by voids in the material or through impurities brought about by contaminants introduced during the manufacturing process. Through constant stress, the inclusions closer to the surface (within 400 μm below the raceway) will branch out and begin to chip away at the exterior. This type of failure is commonly known in the railroad industry as Rolling Contact Fatigue (RCF). Rolling

Contact Fatigue is the main mode of failure in a healthy and properly loaded bearing. Material fatigue is caused by contact stresses, in the example of a bearing it is caused by the rollers contact with the cup and cone raceways. Although material fatigue is primarily due to contact stresses, subsurface inclusions from material impurities can speed the defect development and propagation process.

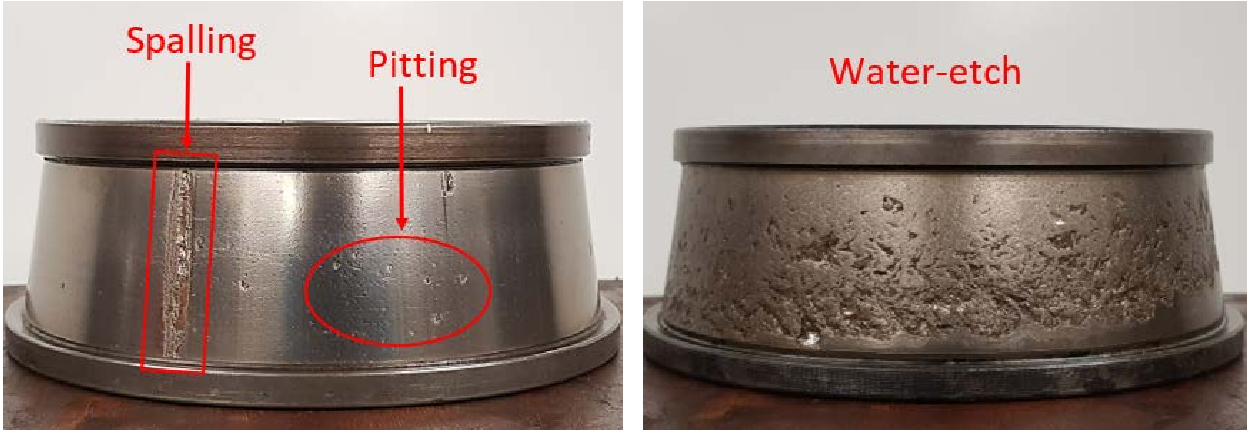

Figure 3. Example of localized defects (left) and distributed defect (right)

1.1.2 Railway Safety

Once a defect develops on a bearing component, the near-frictionless rotational behavior of the bearing is compromised. The steel chipped off through propagation of subsurface inclusions will enter the grease and create a grinding effect on the component raceways as the lubricant continues to circulate through the bearing. Depending on the defect size, increased friction caused by coarse grease can predispose the bearing to frictional heating. The rise in bearing temperature creates a cycle of grease degradation which will cause further friction increase. Although the average calculated operating life of a bearing is more than 3 million kilometers [2], this estimation can drastically decrease in the presence of a developed defect. Unfortunately, defect development is highly variable and subject to the component material and manufacturing processes of the component. If not properly monitored, these defects can become catastrophic, leading to derailments or in-service failures.

1.2 Derailments and In-Service Failures

Equipment-caused train derailments can range from 100 to 150occurrencesper year[3]. Not only are derailments costly, ranging from $25,000 to $250,000 an hour depending on the derailment site, they are also dangerous for both people and the surrounding area. High-risk derailments can cause environmental contamination and will require extensive cleanup. Derailments are the most often heard cases of train failure. However, if following the transportation definition, risk can be thought of as the product of harm and probability. While in-service failures (ISFs) generally have shorter, less costly delays, they occur more frequently than derailments [4].

ISFs take place when the conductor is alerted of an immediate-action-required fault. This urgency prompts the conductor to halt the train in order to receive maintenance or replacement of the defective components. Granted that an ISF is less disastrous than a derailment, ISFs can cause secondary effects that will contribute to their impact. These secondary effects include reactionary delay to other trains in the route or network of the ISF’s transit. Class I railroads have reported over 23,000 equipment caused ISFs in a year, often in response to reactive wayside detectors [4].

1.3 Wayside Condition Monitoring Systems

As an attempt to decrease freight train accidents, wayside condition monitoring systems were developed. Wayside monitoring systems are characterized by the same principle data acquisition method. These systems collect and analyze data obtained from bearings rolling over the detection system. If bearing conditions diverge from the predetermined threshold of a healthy bearing, the conductor is alerted so that appropriate actions can be taken.

1.3.1 Trackside Acoustic Detection System (TADS™)

The Transportation Technology Center Inc. (TTCI) developed TADSTM^{TM} to monitor bearing health through acoustic signatures. TADS^{TM} utilizes microphones to detect severe, high-risk defects in bearings as the train passes through the wayside system. These high-risk defects are termed “growlers” due to the low frequency the large spalled area (over 90% of the component raceway) produces. This system is an example of a reactive wayside detector, as it specializes in diagnosing end-of-life bearings. While TADS^{TM} has a high proficiency in recognizing end-of-life bearings, not all severe defects are detectable through their algorithm and small or initiating defects will not be perceived [5].As of March 2017, only 19 TADS^{TM} are in operation nationwide, meaning that many freight cars can go through their entire service life without encountering one of these systems [6].

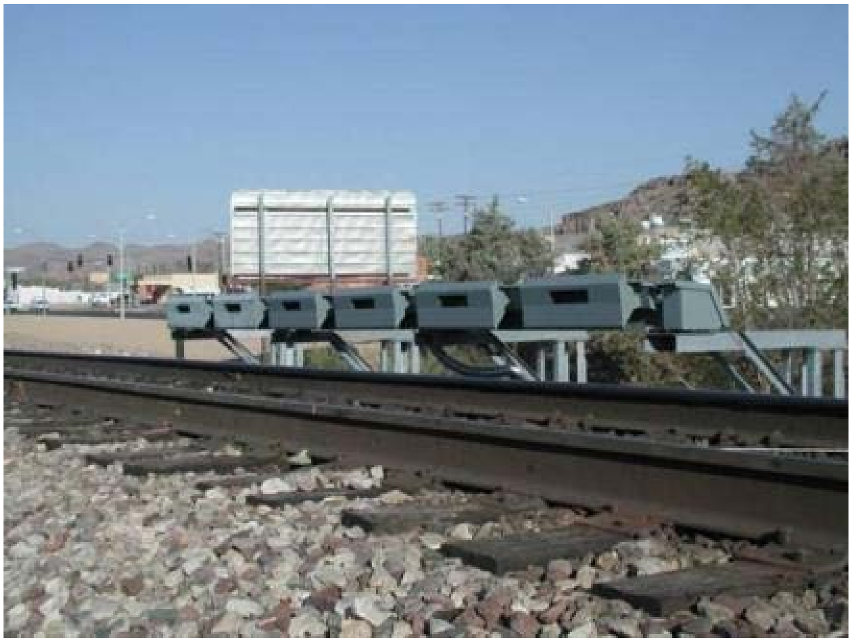

Figure 4. Photograph of a TADS™ site[6]

1.3.2 RailBAM®

In contrast with TADS^{TM}, RailBAM® is a bearing acoustic monitoring system sensitive enough to identify defects initiating on bearing components. This wayside acoustic detector has developed a reliable process for distinguishing severe and developing bearing defects. RailBAM®, shown in Figure 5, can process 200 wagons passing through the system at speeds greater than 50 km/h (30 mph) in less than 10 minutes [7]. Native to southern Australia, only 20 RailBAM® detectors are in operation, causing the same predicament as TADS™ of neglecting railcars not passing through the system's routes [6].

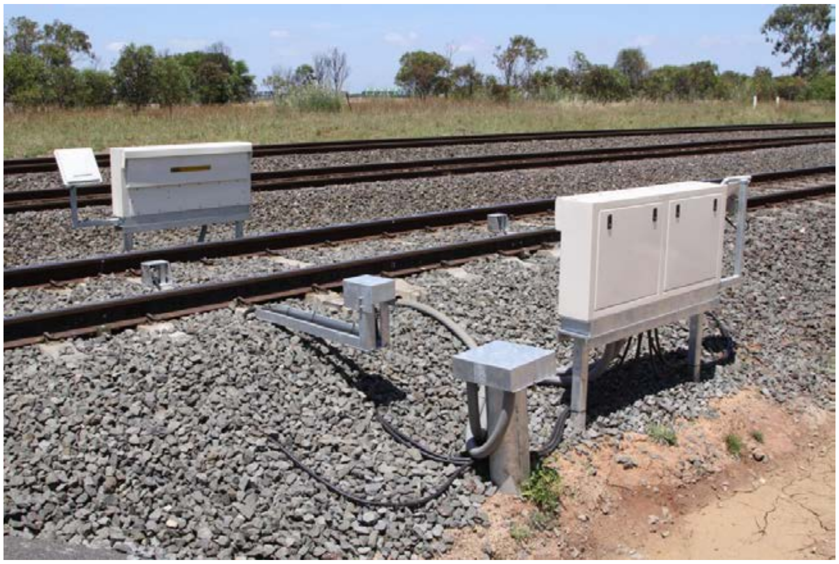

Figure 5. Photograph of a RailBAM® system

1.3.3 Hot-Box Detector (HBD)

Hot-Box Detectors (HBDs) work through a series of infrared sensors that scan bearings, wheels, and brakes as the rail cars pass over the detectors, as shown in Figure 6. If the operating bearing temperatures obtained through the HBD are greater than 76.7°C (138.06°F) above ambient or greater than 35°C (65°F) above the temperature of the bearing that shares the same axle, the train operator will be alerted. HBDs are placed approximately 40 km (25 miles) apart along the track. Over 6,000 detectors can be found across North American railroads, making these detectors the most common form of wayside condition monitoring system in the U.S. Even with the abundance of HBDs, there are still major problems encountered while analyzing this system.

A tapered roller bearing can overheat and may even burn off in just 1 to 3 minutes [6]. Assuming a maximum velocity of 129 km/h (80 mph), it would take a railcar approximately 20 minutes to reach the next HBD. This time interval between detectors gives rise to the possibility of overheated bearing failure. Conversely, at decreased speeds or while awaiting inspection, a bearing can cool down to normal temperatures making it difficult for the operator to properly assess bearing health. HBDs are stationary and have scanning ranges that are predetermined through calculated bearing dimensions for a specific class. As mentioned previously, bearing dimensions, both diameter and width, are subject to change with the bearing class. Varying bearing dimensions cause relative change in the position of the bearing on the axle. This causes the HBD measured temperatures to be inconsistent from actual bearing operation temperatures. Several studies have commented on the unreliability of HBD temperature readings through data acquired from laboratory and field tests [9][10][11].

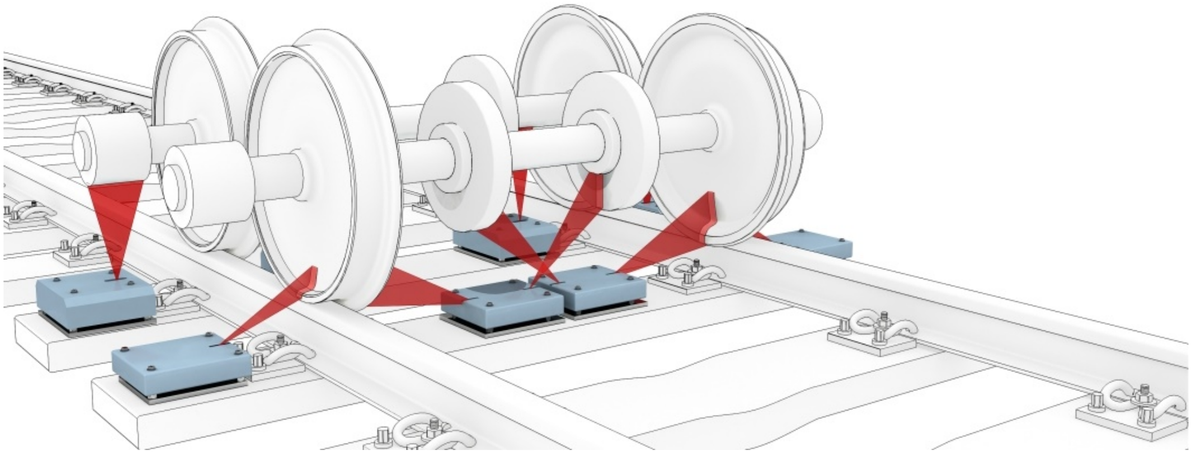

Figure 6. Example of a Hot-Box-Detector (HBD) site[8]

1.4 Onboard Condition Monitoring Systems

The short latency period between fault detection and failure occurrence in bearings creates concern in the use of wayside condition monitoring systems. Onboard fault detection methods were developed to achieve real-time condition monitoring. Onboard monitoring reduces costly reactive maintenance and improves safe transit by providing instant data of rolling stock health. These systems are meant to detect defect initiation and monitor progression to allow proactive maintenance schedules to be developed in order to decrease waste caused by preventative and reactive actions.

1.4.1 SMART-BOLT™

In the late 1900's Carnegie Mellon Research Institute (CMRI) developed a thermal sensor bolt for the continuous monitoring of bearing temperatures. This onboard monitoring system is designed to replace one of the bolts located at the end cap of the bearing, securing itself onto the axle. The location of the bolt was determined in order to minimize the variability of temperature gradients throughout the bearing caused by heating and cooling effects on the contact surface [12].SMART-BOLT™ consists of a battery, thermal-mechanical sensor, piston, and a transmitter. The transmitter is designed to alert the conductor once the bearing reaches the preset alarm temperature of 121°C (250°F). To facilitate inspection, the piston releases an antenna for quick identification of the overheated bearing. However, this antenna requires an authorized party to reset as the thermal actuator locks into place once it has been activated.

Although the normal operating temperature of a bearing is typically 81°C (178°F), bearing temperature trending is a common phenomenon occurring in defect-free bearings that exhibit end-of-life temperatures[13]. The locking mechanism of SMART-BOLT™ prevents continuous monitoring of the bearing in false positive cases. These interruptions make it difficult to obtain a reliable profile of the bearing condition, which would aid in creating proactive maintenance schedules.

1.4.2 Wireless Sensor Node

Wireless sensor nodes (WSN), such as the one developed by IONX shown in Figure 7, provide continuous real-time bearing temperature data to the locomotive engineer. WSNs contain Central Monitoring Units (CMU) which record both the bearing and the current ambient temperature [14]. WSNs use various algorithms to create a trend analysis of the bearing temperatures and provide early warning of possible failure. The CMU transmits this data via satellite or cellular network to the engineer for warranted action.

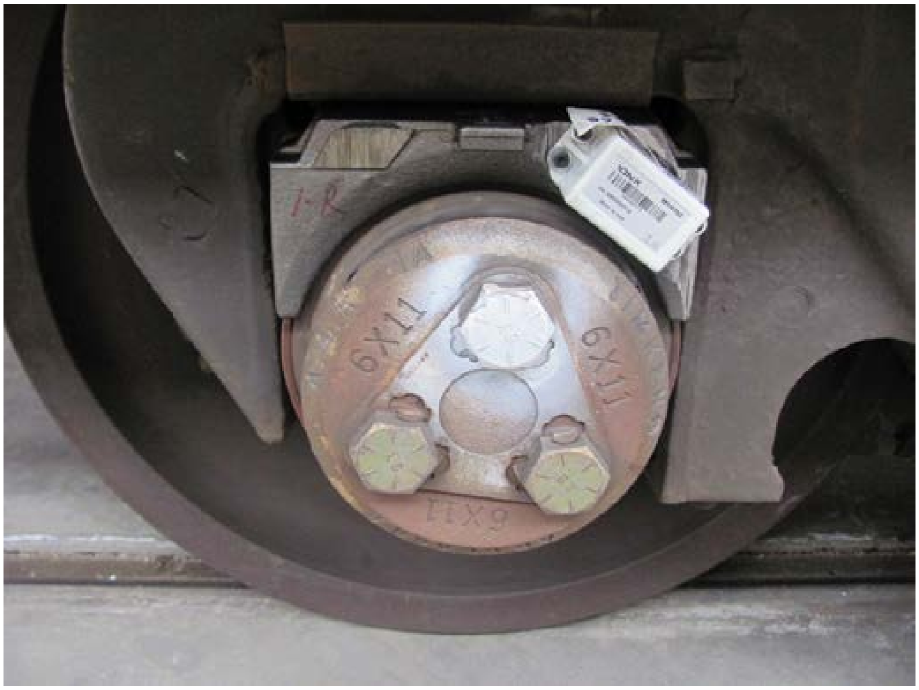

Figure 7. Field installation of a Wireless Sensor Node

1.4.3 Timken Guardian™ Bearing

The Timken Guardian™ Bearing is composed of a radio transmitter, microprocessor, power supply, and sensors placed within the bearing. These sensors monitor bearing conditions such as wheel rotational speed, temperature, and vibration, then proceed to transmit the data wirelessly through radio frequencies sent by the transmitter. The data can be sent either to a receiver on the railcar or store it in an off-site computer for future analysis. Once the receiver has been alerted to a possible defect, the bearing must be disassembled for a thorough inspection to be performed. Being one of the leading forms of bearing health monitoring, Timken Guardian™ Bearings are high-priced. These systems require the purchase of an entire bearing and can cause delays during disassembly and inspection if spare bearings are not available.

1.5 Purpose

Over the past 30 years, the U.S. railroad industry has invested in automated condition-monitoring technology (ACMT). Most wayside and onboard monitoring systems are reactive in nature, alerting only of imminent failure. This technology does very little in preventing ISFs given that immediate action is generally required at the notification of one of these systems. Still, the systems that provide continuous data to alert of onset bearing failure cannot provide remaining service life models. This lack of understanding in spall progression patterns often leads to premature maintenance and removal of tapered roller bearings.

The University Transportation Center for Railway Safety (UTCRS) research group at the University of Texas Rio Grande Valley (UTRGV) has developed a proactive bearing condition monitoring system which can reliably detect bearing defect initiation. The onboard condition monitoring system can continuously assess bearing health and provide accurate, real-time data. The reliability of this system has been validated through several laboratory and field tests at UTRGV and the Transportation Technology Center, Inc. (TTCI).

This system, Smart Adapter™, developed by UTCRS can measure temperature and vibration signatures of a bearing. Smart Adapter™ uses the root-mean-square (RMS) value of the bearing's acceleration to assess health and approximate spall size if a defect is found to be present. Then, an analysis of the frequency domain of the acquired vibration signature serves to locate the defect component location. The size estimated through the RMS value can then be used to predict the residual life of the bearing.

This thesis will focus on the development of a proactive and cost-efficient maintenance cycle for railcar tapered roller bearings using data acquired by Smart Adapter™. The data presented in this thesis can assist in eliminating costly delays and ISFs by proposing spall progression trends of bearing components most prone to deterioration. These trends will be used to provide remaining service life models of railroad rolling stock.

CHAPTER II

EXPERIMENTAL SETUP

The data presented in this thesis was acquired from experiments performed on dynamic bearing testers designed and manufactured by the University Transportation Center for Railway Safety (UTCRS). The testers are housed in the engineering labs at the University of Texas Rio Grande Valley (UTRGV). The four-bearing tester (4BT) can run four class K, F, E, or G bearings simultaneously, while the single-bearing tester (SBT) can accommodate one class K, F, E, or G bearing at a time. The data collected for this study was obtained from laboratory experiments in which only class K and class F bearings were tested. These specific bearing classes were chosen because they are the most widely used in freight rail transportation in the United States and Canada. Moreover, class F and K bearings use the same exact cone (inner ring) assemblies which allows for these components to be interchangeable.

2.1 Bearing Assembly

Class F and class K bearings are fabricated using AISI 8620 steel and the tapered rollers are case-hardened. The main components in these two bearing classes have the same dimensions, with the exception of the outer ring (cup) and the spacer ring. Due to class F cups having a larger width, the spacer ring that separates the cones must also be larger than that used in class K bearings. This causes minor changes in the bearing assembly with respect to the bearing grease lubrication and total weight.

2.1.1 Measurements

Every inner ring (cone) selected requires cage lift, cage shake, and roller spacing measurements to be taken. Cage shake and cage lift are performed with a dial indicator and serve to measure the lateral and vertical motions of the roller cage with respect to the cone. A setup of these measurements can be observed in Figure 8. Roller spacing measurements are carried out by inserting a feeler gauge in the space between the roller and the cage rib. These measurements are used to minimize the possibility of roller skew (misalignment) due to abnormal spacing in the cages holding the rollers against the inner ring. Maximum and minimum lateral measurements of the bearing assembly are also taken with a desired range of 0.023in to 0.028 in. Laterals help determine if the correct spacer ring has been selected. The spacer ring helps keep the bearings spinning parallel to the axle. Otherwise, like the rollers, the bearings might roll skewed, preventing optimum rolling speeds.

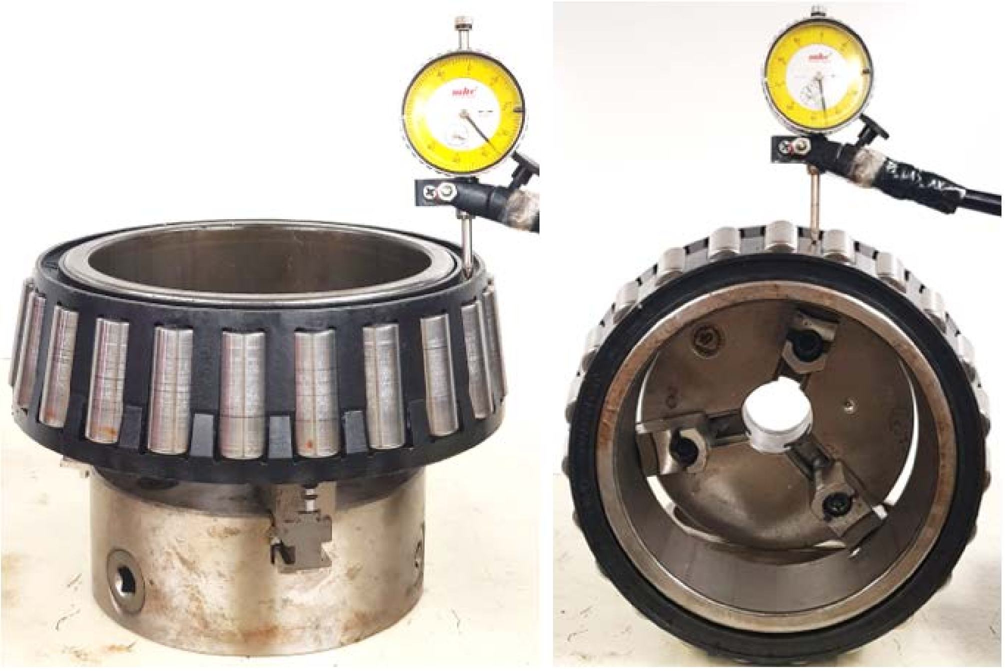

Figure 8. Cage measurement set-up: cage lift (left), cage shake (right)

2.1.2 Lubrication

The near-frictionless rotation experienced by tapered roller bearings is partly attributed to the lubrication it contains. Following the Association of American Railroad (AAR) standards, the bearings are filled with grease in the quantities and regions specified in Table 2. Class K bearings have a dimensional width of 22.9 cm (9 in) while class F bearings have approximately a 30.5 cm (12 in) width. While the cone assemblies are the same, the difference between these two classes of bearings is the spacer ring used. The width of a class K bearing spacer ring is approximately 1.46 to 1.48 cm (0.575 to 0.583 in). Whereas the spacer ring width for a class F bearing is between 3.68 and 3.94 cm (1.45 to 1.55 in). Due to the region of the cup (outer ring) between the two cone assemblies being noticeably smaller in class K bearings, no lubrication is applied to this spacer region for class K bearings.

Table 2. Lubrication (grease)application measurements for class K and class F bearings

Bearing Class	Total Grease [L] / [oz]	Spacer Region Grease [L] / [oz]	Cone Assembly Grease [L] / [oz]
F	0.6506 / 22	0.2662 / 9	0.3845 / 13
K	0.3845 / 13	N/A	0.3845 / 13

Once the bearing has been properly lubricated, it is secured with a grease seal and placed on a scale to measure the total weight. Depending on bearing class the weight can vary from 29.5 kg (65 lb) to 36.3 kg (80 lb). Additional weight can be caused by the cage type used within the bearing cone (inner ring) assemblies. Polyamide cages are significantly lighter than their counterpart steel cages.

2.2 Four-Bearing Tester (4BT)

The four-bearing tester is powered by a 22.4 kW (30 hp) variable speed motor that is controlled via a variable frequency drive (VFD). Through a pulley and its adapter, the motor creates axle rotational speeds that can be translated into track speeds, as shown in Table 3. A hydraulic cylinder is used to apply loads of up to 150% of full load, with full load corresponding to a force of 153 kN (34.4 kips) per class F or K bearing. Notice in Figure 9, which depicts the four-bearing tester, the hydraulic cylinder applies vertical load directly on bearing 2 (B2) and bearing 3 (B3). Therefore, a total of 306 kN (68.8 kips) are applied to the two middle bearings (153 kN or 34.4 kips per bearing) with the reaction forces also applying 153 kN (34.4 kips) on each of the outer bearings (B1 and B4). In order to replicate field service operating conditions, only data acquired from the two middle bearings (B2 and B3), which are top loaded, were used in this study.

Table 3. Axle to Track Speed Conversions

Axle Speed [rpm]	**Track Speed [mph] / [km/h]**
280	30 / 48
327	35 / 56
373	40 / 64
420	45 / 72
467	50 / 80
498	53 / 85
514	55 / 89
560	60 / 97
618	66 / 106
699	75 / 121
799	85 / 137

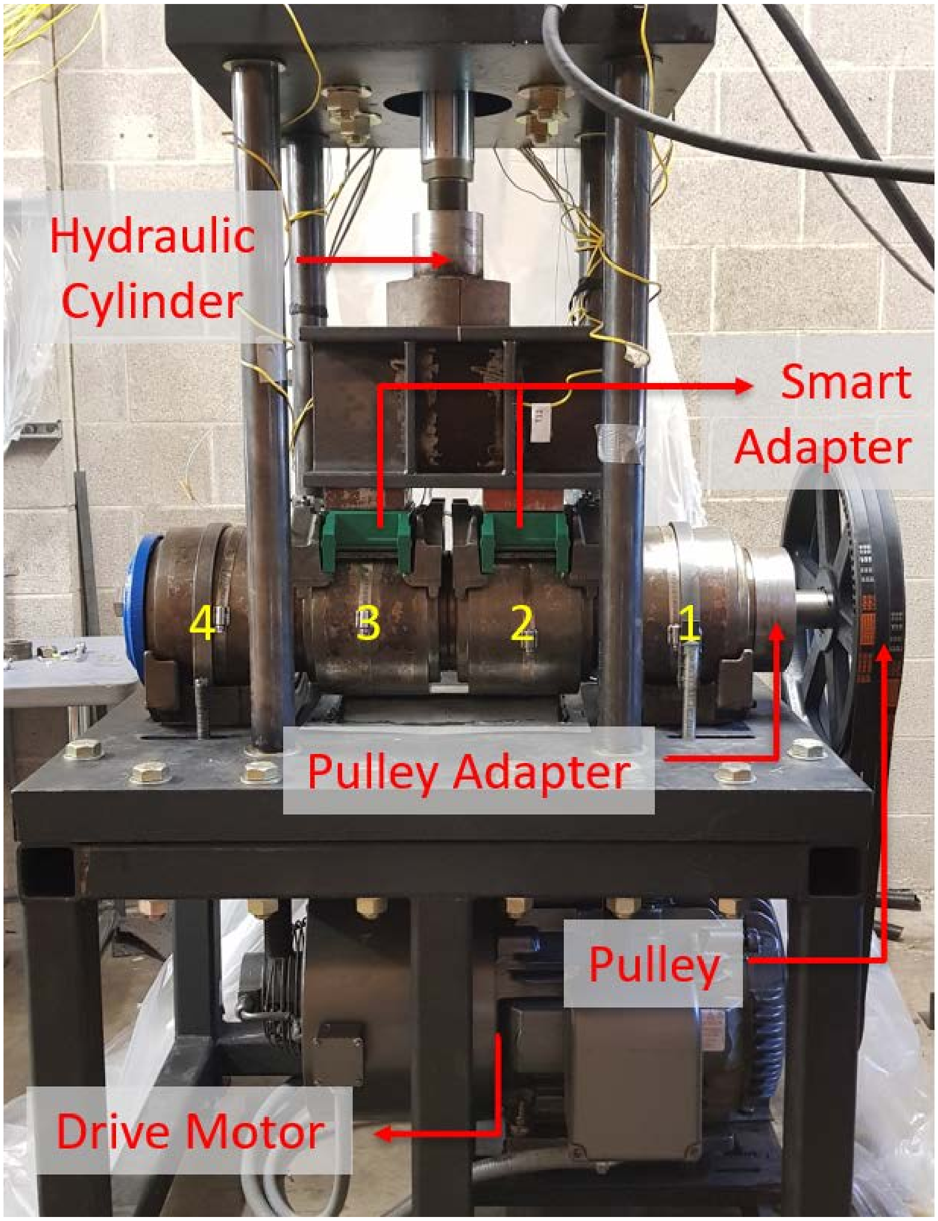
Hydraulic Cylinder
Smart Adapter
4
3
2
1
Pulley Adapter
Pulley
Drive Motor

Figure 9. Four-Bearing Tester (4BT)

For this study, it was necessary to track and record the temperature and vibration signatures of the test bearings. To do so, the steel adapters were machined to accept two 70g accelerometers placed in the outboard SmartAdapter^{TM} (SA) and mote (M) locations, along with one 500g accelerometer placed in the outboard radial (R) location. To monitor the bearing operational temperature, the adapter was outfitted with two bayonet thermocouples placed in the middle of each raceway, and one regular K-type thermocouple that was held tightly against the middle of the outer ring (cup)utilizing a hose clamp. The modified adapter displaying the accelerometer (right) and thermocouple (left) locations is pictured in Figure 10.

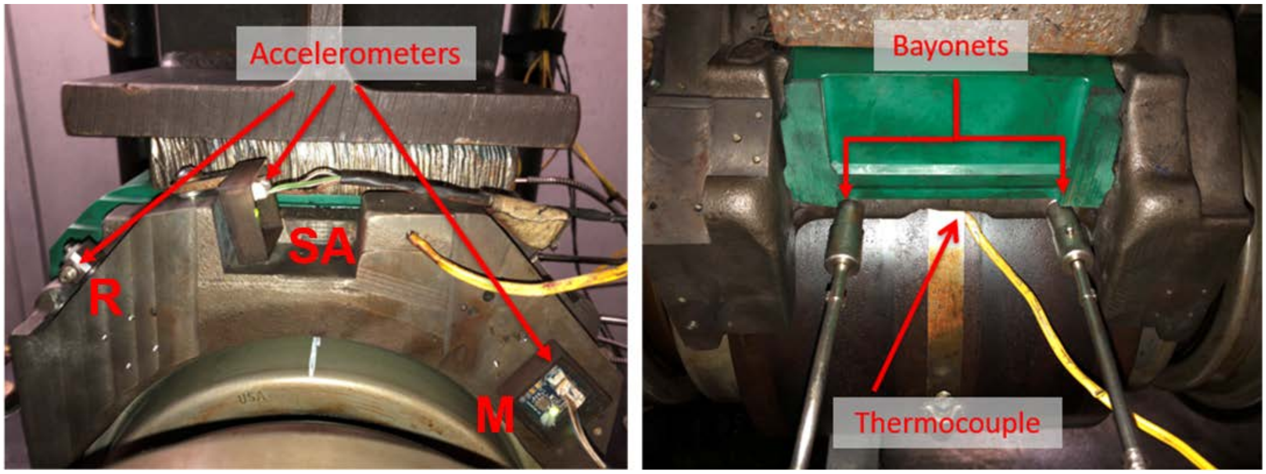

Figure 10. Modified 4BT adapter showing vibration sensors (left) and temperature sensors (right)

Two industrial size fans were used to simulate the convective cooling that bearings in field service experience due to crosswind passing over the bearings while the train is in motion. The fans generate average airflow speeds of approximately 6 m/s (13.4 mph). A schematic of the fan and 4BT layout is presented in Figure 11. The specially constructed, temperature-controlled environmental chamber which houses the 4BT is equipped with a commercial freezing unit with a cooling capacity of 7.6 kW (10.2 hp). The chamber can simulate a wide range of ambient temperatures with lows of -40°C (-40°F) and highs of as much as 65.6°C (150°F). This allows the four-bearing tester to mimic the extreme ambient conditions that might be experienced during service across routes in various seasons and climates.

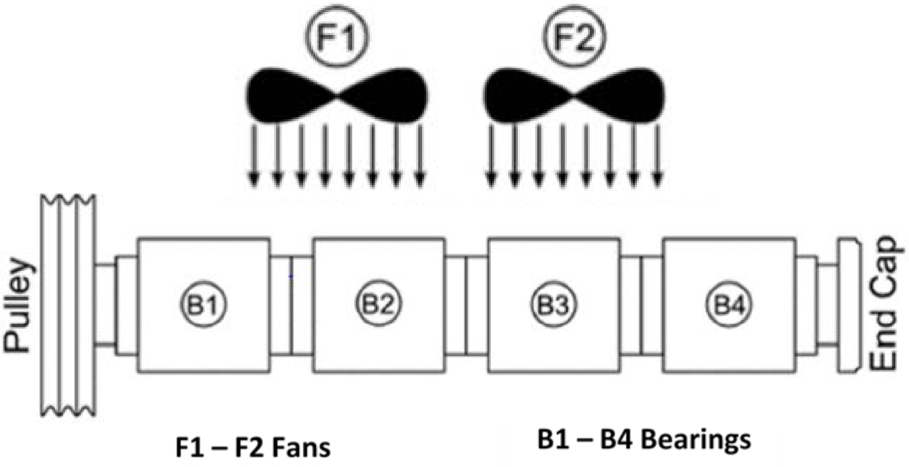

Figure 11. Top view of four-bearing tester (4BT)

2.3 Single-Bearing Tester (SBT)

The single-bearing tester (SBT) is designed to hold a single class F or class K bearing on a specially fabricated 4140 steel axle. The main objective of the cantilever design of the single bearing tester, which can be seen in Figure 12, is to accurately reproduce field service operating conditions. Similar to the 4BT, the SBT is equipped with a22.4 kW (30 hp) variable speed motor, capable of providing the operational speeds listed in Table 3. A hydraulic cylinder, identical to that of the 4BT, is used to apply vertical loads. However, unlike the four-bearing tester, the single bearing tester can also apply lateral and impact forces which can be used to mimic the field service conditions of a railcar experiencing hunting and/or wheel impacts or passing over bad rail track segments. The SBT can provide maximum lateral loads of up to 22 kN (5 kips) and maximum vertical loads of up to 222 kN (50 kips).

Another feature of the cantilever design of the SBT is that it allows for easy installation and removal of the test bearing. Thus, the single-bearing tester was primarily utilized to run experiments on bearings having spalls with areas larger than 6.45 cm^2 (1 in^2). These larger spalls require frequent disassembly and visual inspection to be carried out to closely track defect progression.

Aside from two industrial size fans supplying convective cooling, as those used on the four-bearing tester, the SBT employs a specially designed cooling system fabricated by the UTCRS research team. The setup allows for chilled water to run over the pillow blocks which house the support bearings. The purpose of incorporating this system is to prevent the tester's support bearings from overheating during an experiment.

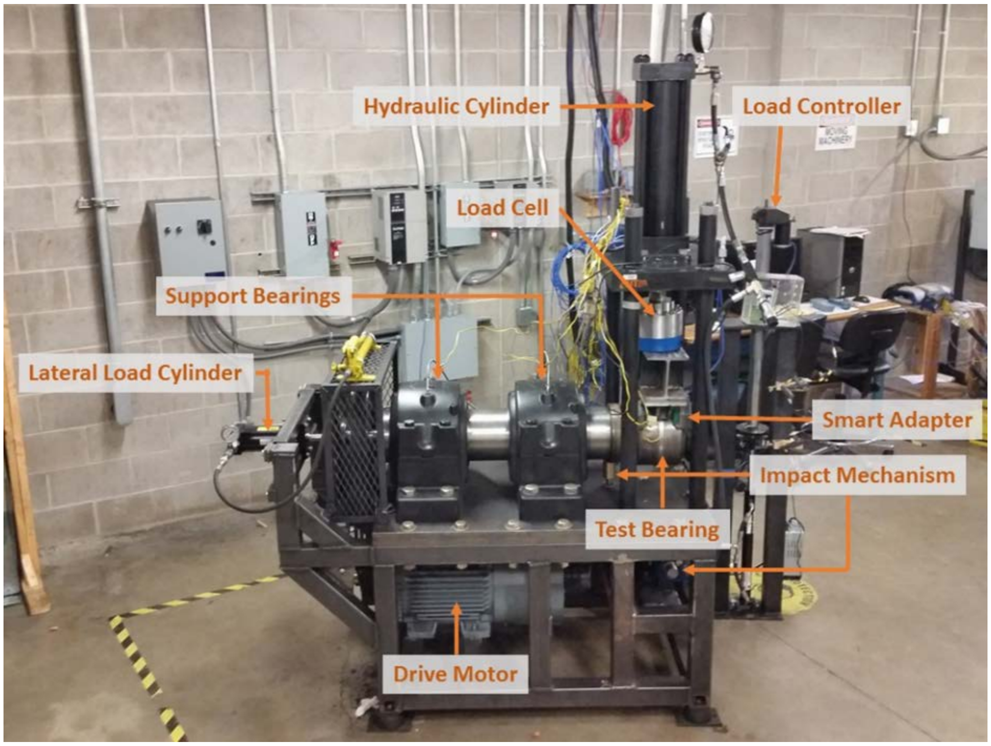
Hydraulic Cylinder
Load Controller
Load Cell
Support Bearings
Lateral Load Cylinder
Smart Adapter
Impact Mechanism
Test Bearing
Drive Motor

Figure 12. Single bearing tester (SBT)

Again, the steel adapter was machined to accept vibration and temperature sensors. For vibration monitoring, four 70g accelerometers were placed in the SmartAdapter^{TM} (SA) and mode (M) locations at both the inboard and outboard sides of the bearing, along with one 500g accelerometer in the radial (R) location on the outboard side. Temperature data was acquired through two inboard and two outboard bayonet thermocouples affixed to the bearing adapter.

Additionally, seven K-type thermocouples were held via a hose clamp around the circumference of the bearing. The bearing thermocouple locations are shown in Figure 13.

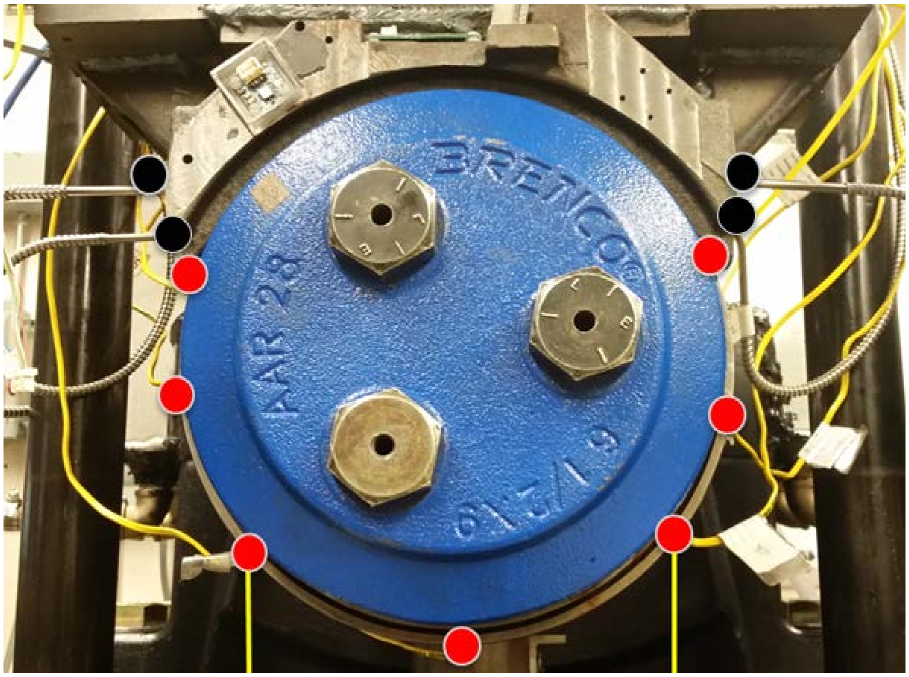

Figure 13. Single bearing tester thermocouple locations: bayonets represented by black dots,K-type thermocouples represented by red dots

2.4 Data Acquisition

LabVIEW™ was used to program of a National Instruments (NI)cDAQ-9174 data acquisition (DAQ) system utilized to log vibration and temperature signatures received from the test bearings. Temperature data was obtained from the thermocouples every 20 seconds for half a second at a sampling rate of 128 Hz. K-type thermocouples were connected to the NI 9213 temperature card of the DAQ to collect the bearing temperature profiles. Vibration signature acquisition was performed through accelerometers connected to a combination of 8-channel NI 9239, NI USB-6008, and NI 9234 cards via 10 - 32 coaxial jacks and BNC connections. The accelerometers collected vibration data every ten minutes for 16 seconds with a sampling rate of 5,120 Hz.

CHAPTER III

DEFECT DETECTION, SPALL MAPPING, AND SPALL GROWTH

The University Transportation Center for Railway Safety (UTCRS) research team has acquired bearing vibration and temperature profiles of operating bearings for over twelve years now. The data presented for defective bearings comes from two primary sources: service-life tested bearings and bearings removed from field service. Service life testing was performed with defect-free bearings that contained at least one subsurface (≤ 600 µm) inclusion after being ultrasonically scanned [15]. All service life testing of defect-free bearings was carried out exclusively on the four-bearing tester (4BT) until a defect (i.e., spall) developed. As a result, the mileage leading to the development of a spall in a bearing undergoing service life testing was known precisely.

The majority of the bearings removed from service were pulled from freight railcars due to defective wheelsets, and upon visual inspection were found to have relatively small inner ring (cone) or outer ring(cup) defects (less than 6.45 cm^2 or $1in^2$). It is important to note that defects with areas below 6.45 cm^2 ($1in^2$) are seldom, if at all, detected by current wayside condition monitoring detectors. The removed bearings did not trigger any wayside detectors and there was no notion of an existing defect, thus the mileage leading to the development of the spall cannot be determined.

While the distance traveled leading to the formation of the spall can be accurately tracked for bearings that underwent service-life testing in the laboratory, it is impossible to obtain the pre-spall mileage for bearings that have been removed from field service. The initiation of a spall is greatly influenced by the material purity and quality and the manufacturing process used. Each component has material impurities and subsurface inclusions that are unique to the component. Thus, a large variance in the spall initiation mileage of a tapered roller bearing component is expected. Consequently, to permit the integration of data from both sources of bearings, the mileage prior to the initiation of a surface defect was not factored in the model development. Hence, the developed models are functions of the distance traveled after a component has developed a spall (defect), where the initial spall formation is taken as the zero-distance reference point.

3.1 Defect Detection

The defect detection algorithm developed by Gonzalez [16] can detect, with 95% accuracy, the onset and propagation of tapered-roller bearing raceway defects. The algorithm is activated when operating speeds are above 65 km/h (40 mph) or when the bearing's operating temperature surpasses 93°C (200°F). Once the accelerometer is triggered, the algorithm will go through three levels of analysis to provide information pertaining to the bearing condition including the presence of any spalls (defects), defect classification, and approximate defect size.

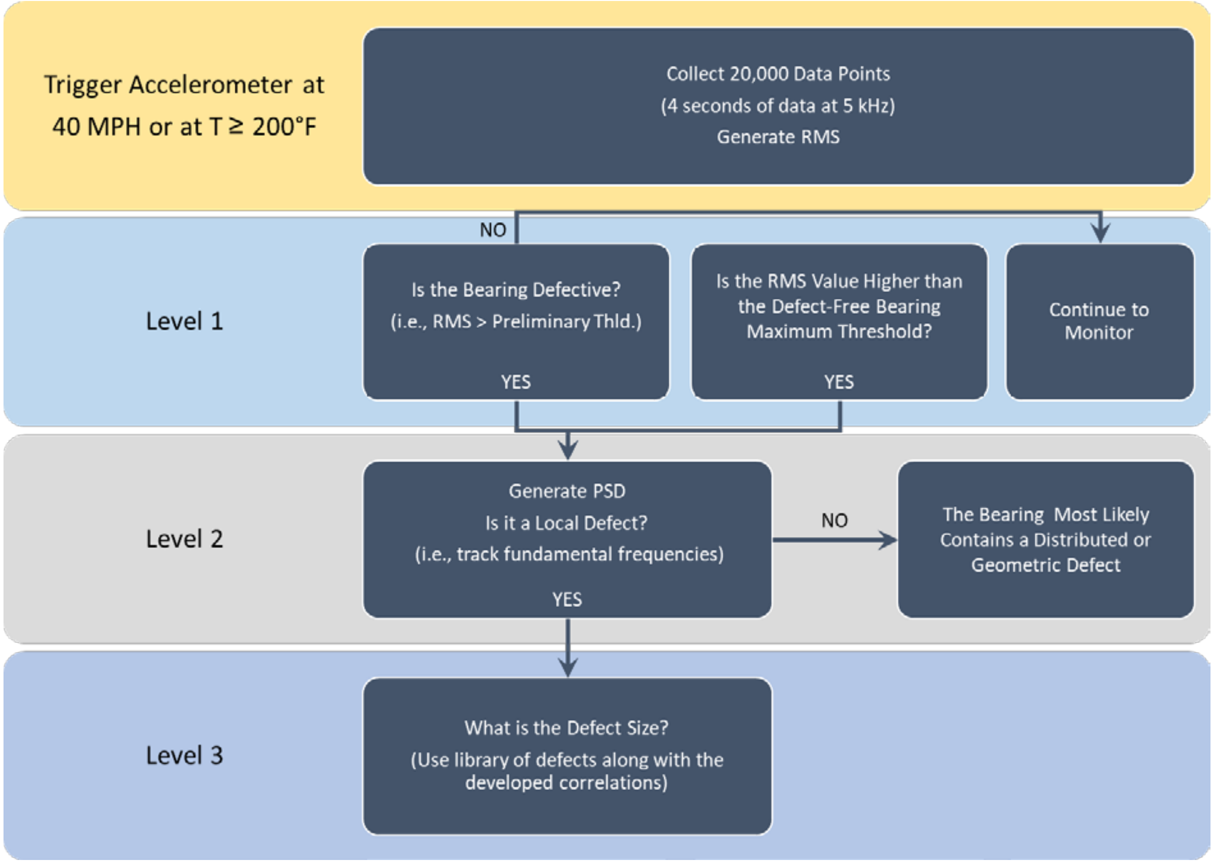
Trigger Accelerometer at 40 MPH or at T ≥ 200°F
Collect 20,000 Data Points
(4 seconds of data at 5 kHz)
Generate RMS
NO
Level 1
Is the Bearing Defective?
(i.e., RMS > Preliminary Thld.)
YES
Is the RMS Value Higher than the Defect-Free Bearing Maximum Threshold?
YES
Continue to Monitor
Level 2
Generate PSD
Is it a Local Defect?
(i.e., track fundamental frequencies)
YES
NO
The Bearing Most Likely Contains a Distributed or Geometric Defect
Level 3
What is the Defect Size?
(Use library of defects along with the developed correlations)

Figure 14. Defect detection algorithm flowchart [16]

Level 1 analysis is the first step in the three-tier algorithm and serves to identify whether the bearing is healthy (defect-free) or defective. Years of data collected from bearing testing and vibration monitoring, a margin for healthy bearing vibration signatures was determined. This threshold establishes the maximum possible vibration levels within a defect-free bearing at simulated train speeds ranging from 48 km/h (30 mph) to 137 km/h (85 mph). If the vibration levels within a bearing, as measured by the root-mean-square (RMS) values of the acquired vibration data are higher than the maximum threshold at a specific speed, the bearing is identified as defective and the algorithm proceeds to Level 2 analysis.

Categorization of the defect type present in a tapered-roller bearing is done in Level 2 analysis. As mentioned earlier, there are three defect classifications: localized, geometric, and distributed. Level 2 is mainly a frequency-domain analysis where power spectral density (PSD) plots are generated. These PSD plots are then analyzed to obtain the fundamental bearing frequencies and their harmonics. The railroad tapered roller bearing fundamental frequencies are described in detail in reference [16]. In Level 2 analysis, these fundamental rotational frequencies are tracked and used to find the corresponding defect frequencies for the outer ring (cup), inner ring (cone), and roller, as well as their harmonics. A localized defect in one of these components manifests as high peaks at the corresponding defect frequency and its harmonics in a PSD plot, thus, alerting of a localized defect in that component. If a localized defect is identified in Level 2 analysis, the algorithm will proceed to Level 3 analysis. However, if none of the three defect frequencies (cup, cone or roller) and their corresponding harmonics display dominant behavior, yet RMS value calculated in Level 1 analysis is higher than the maximum threshold for health bearings, then the defect is either a geometric or a distributed defect. In his case, the algorithm does not proceed to Level 3 analysis.

Level 3 analysis provides an estimate of the localized defect area(size) for the defective bearing component identified in Level 2 analysis. Level 3 analysis relies on previously developed vibration data correlations to obtain good estimates (generally within 10%) of the defect area. The defect size correlations for the outer ring (cup) and inner ring (cone) produced by Gonzales are shown in Figure 15 and Figure 16, respectively. These defect size correlations were later enhanced by Montalvo [17]. A correlation for the rollers was not developed due to the infrequency with which a roller defect occurs in rail service unaided by the spalling of its surrounding components.

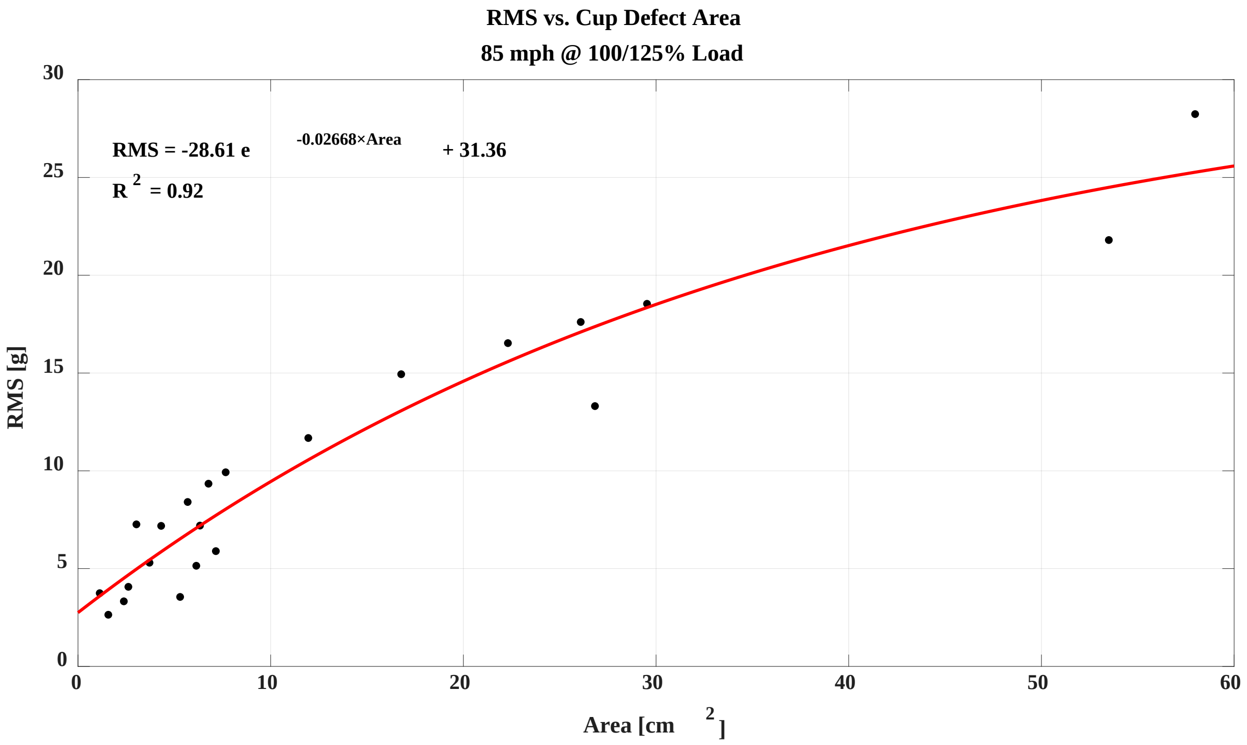

Figure 15. RMS - Cup defect size correlation at 137 km/h (85 mph) and full load[16]

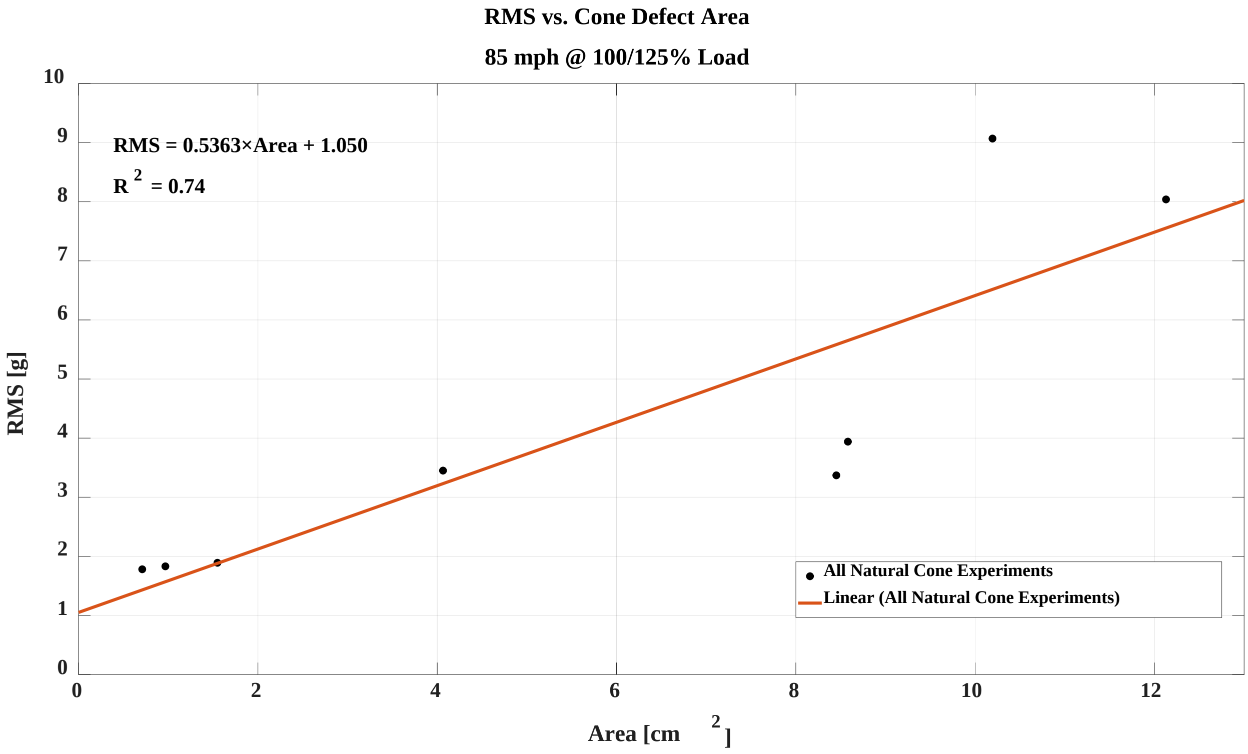

Figure 16. RMS - Cone defect size correlation at 137 km/h (85 mph) and full load[16]

3.2 Spall Casting

Once the vibration monitoring algorithm alerts of signatures above the threshold for a healthy bearing, the experiment is stopped, the bearing is disassembled, and each component is visually inspected. If a defect has developed or a spall has propagated, the area is cleaned thoroughly and surrounded with sealant tape (capable of withstanding a maximum temperature of 204°C or 400°F). After the sealant tape creates a mold around the defect area, a molten bismuth alloy with a melting temperature of 80°C (176°F) is poured into the sealant tape frame enclosing the spall. The casting process is depicted in Figure 17. These casts help keep a reliable record of the spall areas and their progression when the bearing is reassembled and pressed onto the test axle for further defect propagation.

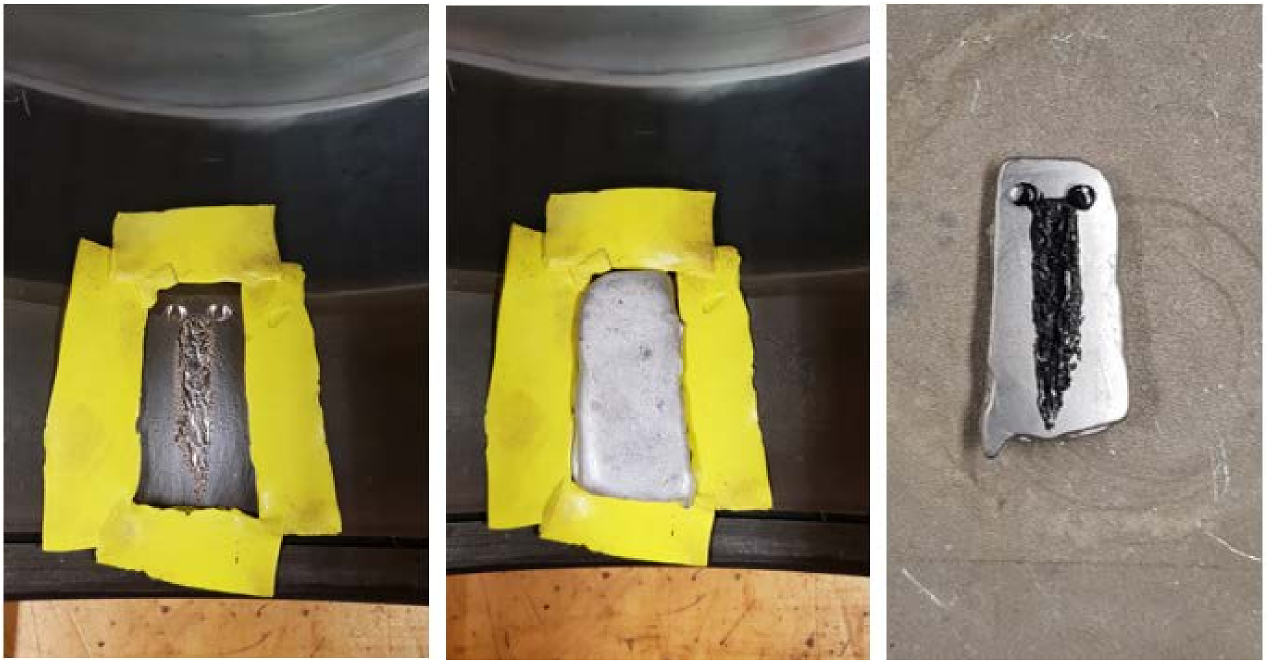

Figure 17. Casting procedure using sealant and bismuth tape

The spalled portion of the cast is painted to mark a contrast between the defect area and the surrounding mold. A photograph is taken of the painted cast alongside a ruler and uploaded to MatLab® where a code was written to create a monochromatic image of the photograph. This post-processed image is then imported to Image Pro-Plus® to perform digital analysis of the defect region. Using the ruler in the image as reference, Image Pro-Plus® uses optical techniques to report accurate defect area parameters in an Excel sheet. The Excel sheet provided by Image Pro-Plus® is transferred to a spreadsheet where test experiment data is compiled. The spreadsheet provides comprehensive data regarding mileage, vibration signatures, spall area, and defect growth.

3.3 Spall Growth Patterns

Defect area and mileage data were analyzed in order to observe the spall growth behaviors. Variables such as raceway and component location as well as defect size were studied. Several patterns in the development of a spall have been observed, especially in relation to the size and location parameters. While the orientation of the subsurface inclusion might be of consequence to spall progression patterns, the bearings removed field service do not have a documented history of being ultrasonically scanned and therefore, the existence and orientation of any surface inclusions cannot be verified. Therefore, subsurface inclusion orientation was not one of the factors considered in this study.

Spall raceway locations can be categorized into three underlying types: edge, center, and full-width [18].The most common raceway spalling location is the edge, shown in Figure 18 (left). Although edge spalls can occur on either border of the raceway, inner ring (cone) defects will generally develop on the smaller diameter rim while many outer ring (cup) defects will develop in the larger diameter segment of the raceway. This edge defect pattern is attributed to stress “flow lines” crowded together in the rib zone. Center spalls, as the one depicted in Figure 18 (center), are less typical than edge defects on account of the rib-roller stresses experienced on the raceway leading to edge spalling prominence [19]. A spall will initially propagate along the width of the raceway until both roller/rib contact borders are reached, exemplified by the full-width spall in Figure 18 (right). Once the edges are reached, the spall will expand circumferentially along the component raceway.

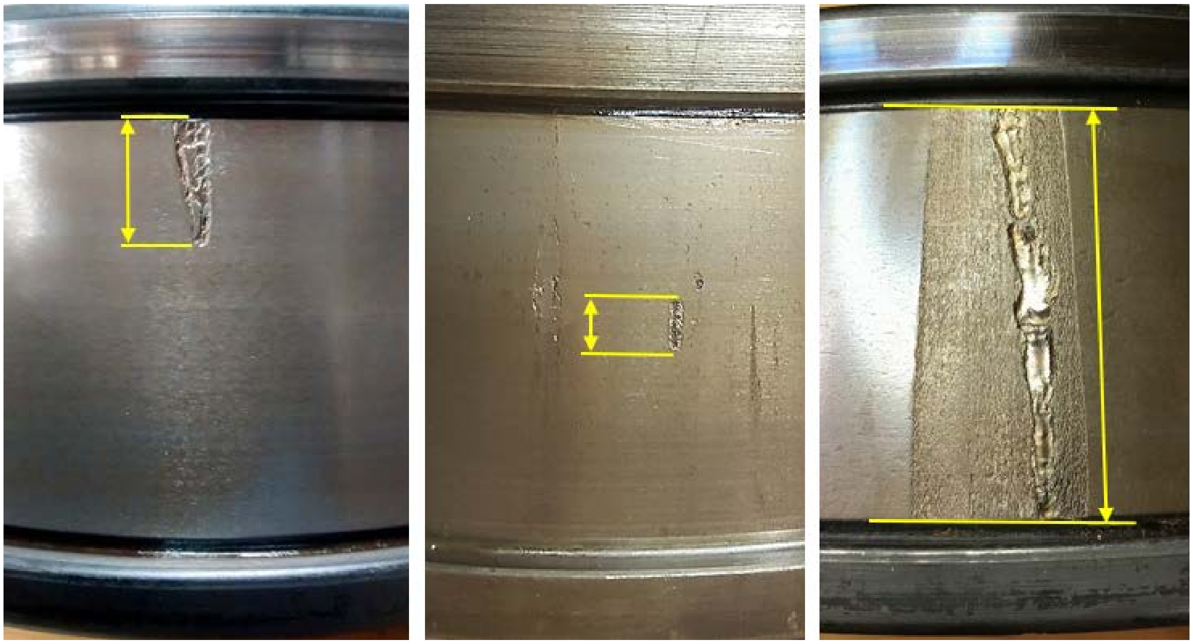

Figure 18. Spall regions depicted in inner rings: edge (left), center (center), full-width (right)

Whereas the growth patterns mentioned are attributed to both inner ring (cone) and outer ring (cup) components, there are differences in the propagation models of these elements that should be noted. The width of an outer ring raceway is approximately5.513 cm (2.170 in), making it larger than the 4.984 cm (1.962 in) corresponding to an inner ring raceway. However, the most prominent difference between these two components is their loading cycles. As previously mentioned, the outer ring (cup) is a static component causing the loaded region to experience periodic cycling stresses over a limited area of the cup raceway. The inner ring (cone) cycles in and out of the loaded zone creating less frequent cyclic stresses in the whole cone raceway.

3.3.1 Inner Ring (Cone)

A noticeable trend is observed when correlating the defect area with total distance traveled, shown in Figure 19. The dash-dotted line across 6.45 cm^2 (1 in^2) marks a transition boundary between two different growth mechanisms for inner ring defects. This critical area for the transition is approximately 6.5 cm^2 (approximately 1 in^2) Findings demonstrate that cone spalls with areas larger than the threshold will grow faster than those below the threshold [20]. In addition to the accelerated deterioration, the mechanisms of growth for larger spall areas displays less variation (R^2=0.86) in growth-rates than is seen in spall areas below the threshold which show higher variation in growth rate and a poorer match to the linear fit (R^2=0.38).

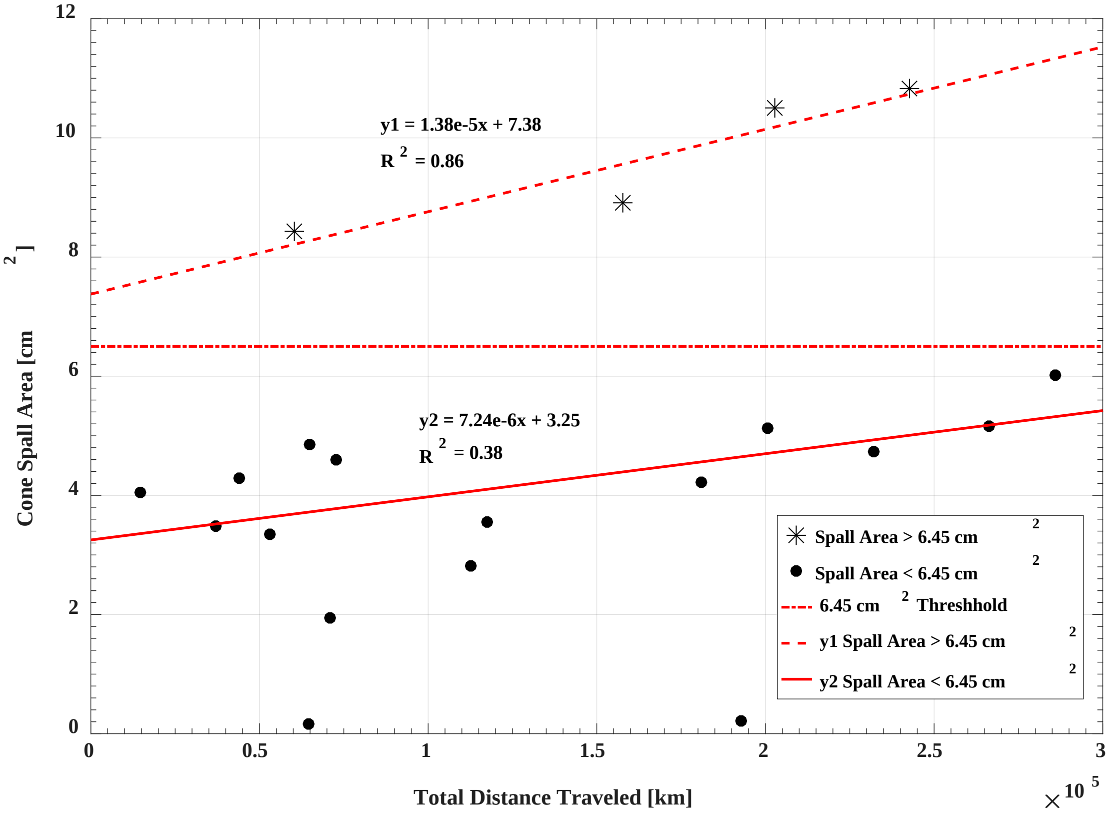

Figure 19. Cone spall size vs total distance traveled [20]

The variation in the deterioration models above and below the designated threshold can be attributed to the growth pattern of tapered-roller bearing defects. As stated earlier, surface defects will initially grow across the width of the raceway due to the roller contact area stresses with a much lower growth rate along. Once the entire raceway width has been covered, spall growth ceases to be multidimensional and continues only in the lateral or raceway direction.

With the loss of shoulders which prevent full roller contact with the bottom of the spall, the mechanisms of growth are reduced to a single mode of growth along the raceway. The single mechanism of growth experienced by larger, above-threshold, defects covering the raceway width explains the decreased divergence seen in the regression analysis. The tendency for spalls to grow preferentially across the raceway is consistent with the higher stresses which are experienced by the spall shoulders in that direction under roller contact. The roller will still be nearly fully supported as it contacts the shoulders on the raceway direction side of the spall while the cross-raceway shoulders will see higher contact stresses as the roller bridges the spall.

3.3.2 Outer Ring (Cup)

The outer ring defect propagation model, shown in Figure 20, presents the spall area as a function of the total distance traveled. Like the cone spall growth data, this graph exhibits two distinct growth rates between spall areas above and below a threshold which in his case is approximately 12.9 cm^2 (2 in^2). Defect areas larger than the threshold have a markedly faster growth rate and show a better fit ($R^2=0.81$) to the regression model as was observed with the cone spalls. The explanation for the difference in slope and divergence of these two propagation patterns is similar to that for the cone (inner ring) components. Again, the spall will primarily grow along the width of the raceway, with slight lateral growth. As the defect reaches the boundaries of the raceway its growth will decelerate. After the defect has spanned the entire width of the raceway, the spall can propagate laterally along the raceway.

Another factor which may contribute to the two distinct defect growth rates and accelerated deterioration of larger defects is the fact that larger spalls in the raceways allow the roller to fully enter the defect depression and make contact with the bottom of the spall. When passing over the defect cavity, the roller engages the spall shoulder creating lateral loads as opposed to those typically observed during the vertical contact stresses. The lateral loads experienced by larger spalls will increase the subsurface shear stress which may lead to faster growth rates.

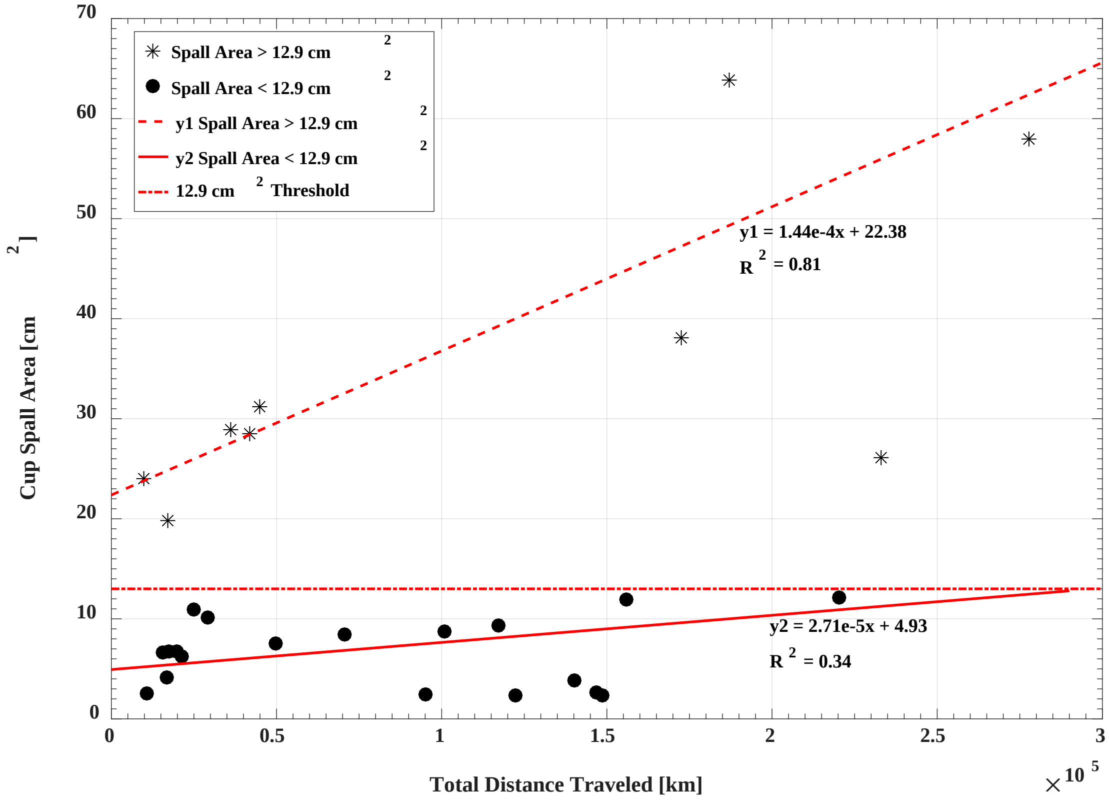

Figure 20. Cup spall size vs distance traveled [20]

In spite of the inner ring (cone) and outer ring (cup) having similar spall growth trends, the primary difference observed between Figure 19 and Figure 20 is the threshold area. This variation in the threshold area for these two models is attributed to the roller contact area in the components [20]. The cone, a convex surface to the roller, will experience approximately 10% smaller contact areas than the concave surface provided by the outer ring (cup) raceway. A visual representation of these geometries is provided in Figure 21. When calculating the Hertzian contact stress, a smaller contact area yields a larger depth of max shear stress as well as 10% higher maximum Hertzian contact stresses **Error! Reference source not found.**.

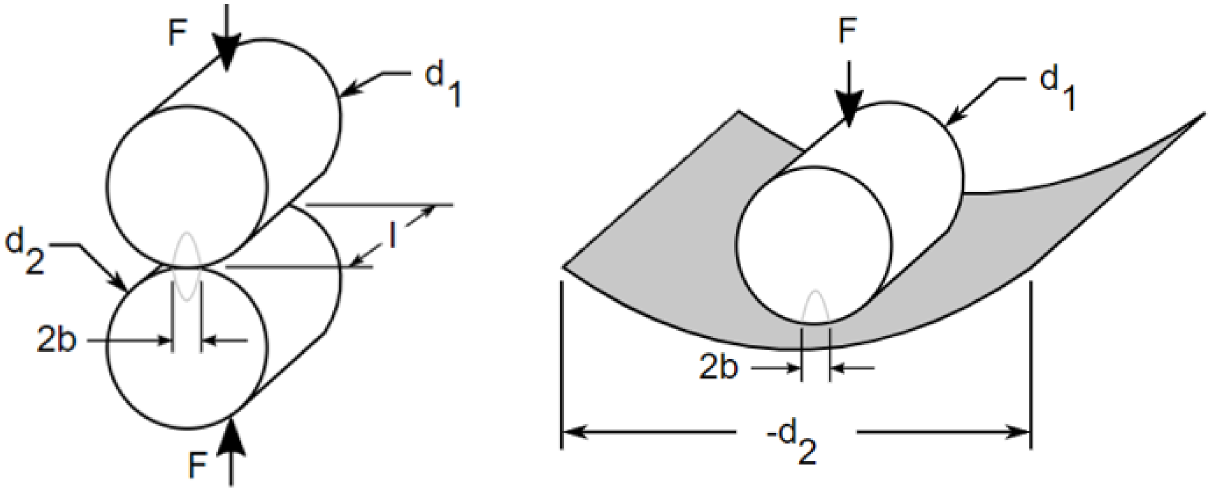
F
d1
d2
l
2b
F
F
d1
2b
-d2

Figure 21. Contact area models: convex inner ring (left), concave outer ring (right)

CHAPTER IV

RESULTS AND DISCUSSION

The residual life models developed for a defective tapered roller bearing component, along with demonstrations of their effectiveness, will be presented in this chapter. Outer ring (cup) and inner ring (cone) data utilized to create these models was obtained from experiments performed over the past decade by the University Transportation Center for Railway Safety (UTCRS). To ensure reliable RMS data, vibration and temperature profiles were obtained from loading conditions of 100 – 125% and speeds ranging from 121 – 137 km/h (75 – 85 mph). RMS and temperature values provided are the average of the readings taken from the last two hours of the experiment. For experiments performed on the four-bearing tester (4BT), readings from the SmartAdapter^{TM} (SA) accelerometer were considered, whereas, for tests conducted on the single bearing tester (SBT), the RMS values obtained from the inboard and outboard SA locations were averaged. Even though the mote (M) location accelerometers were monitored and recorded, they were not used in this study because the SA location accelerometers have been proven to provide more accurate and reliable vibration levels within bearings.

4.1 RMS and Defect Area Correlation Models

Continuous laboratory testing of defective bearings has allowed for the enhancement of the previously developed RMS versus defect area correlation models shown in Figure 15 and Figure 16. The cup (outer ring) defect area versus RMS regression model, presented in Figure 22, maintained an exponential trend while exhibiting an increase in the Goodness-of-Fit R^2value to 0.93. A more significant improvement was observed in the inner ring (cone) correlation, given in Figure 23, which, while retaining its linear form, increased from an R^2 value of 0.74 to and R^2 value of 0.94.While the cup and cone correlations maintained their original trends, the equations were slightly modified to conform with the new data points acquired from the recent laboratory testing.

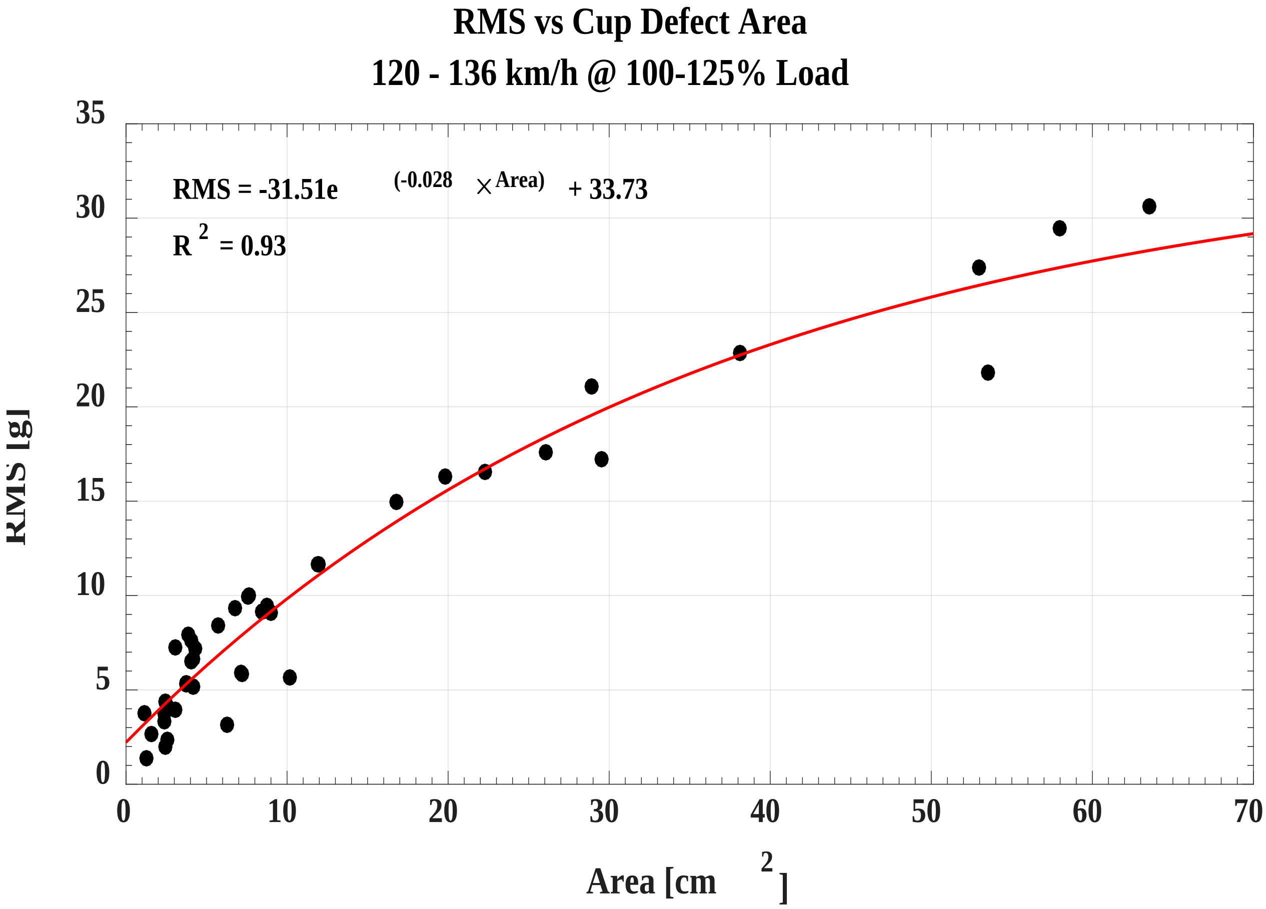

Figure 22. Improved regression analysis of RMS vs cup spall area

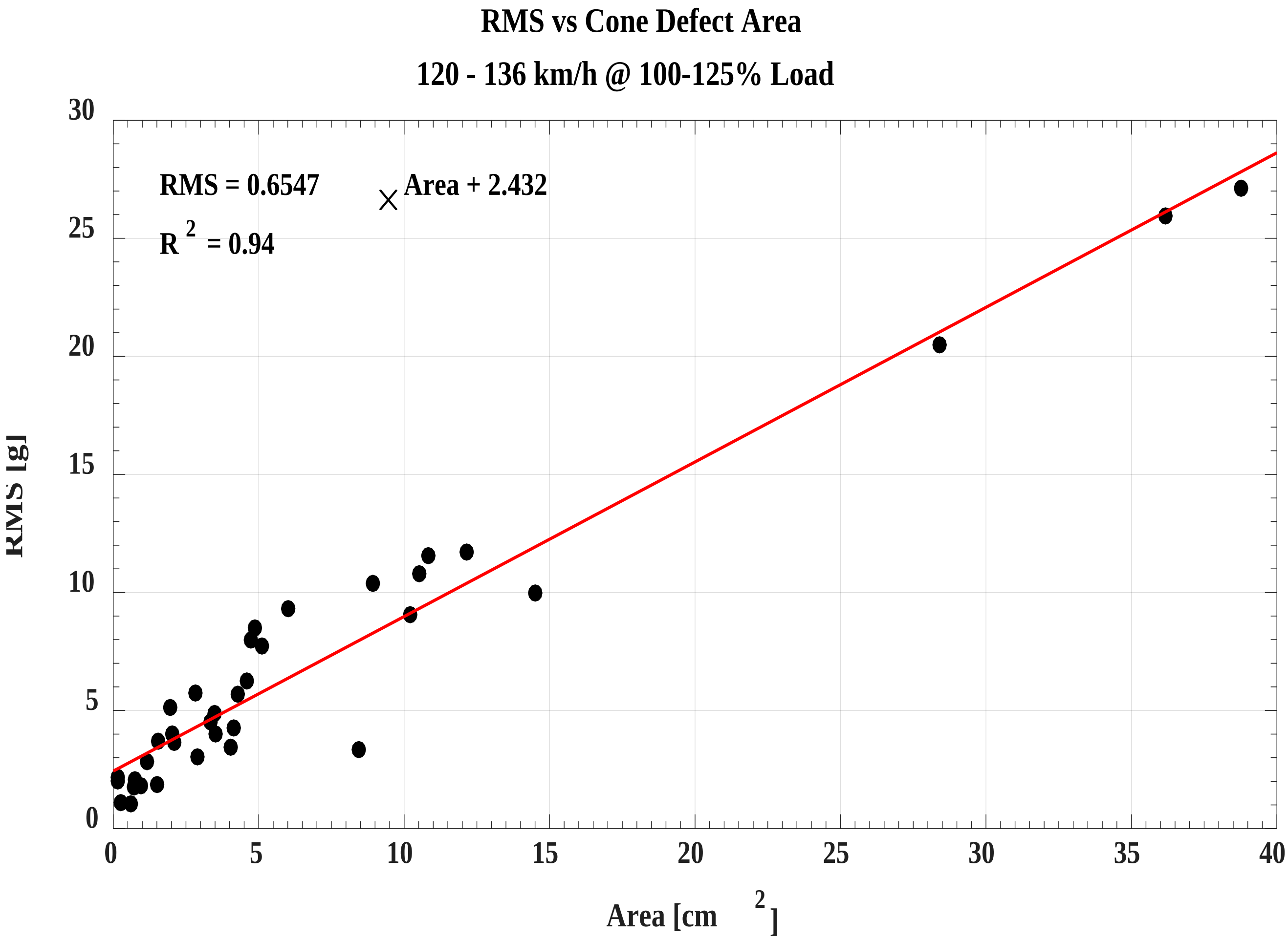

Figure 23. Improved regression analysis of RMS vs cone spall area

The enhanced regression models developed for the bearing component defect size (area) as a function of the vibration levels as measured by the RMS values, presented in Figure 24 for cups and Figure 25 for cones, were categorized in terms of the defect severity, as shown in Table 4. The RMS ranges listed in Table 4are the result of the wealth of experience in defect deterioration patterns gained through the extensive laboratory testing carried out by the UTCRS research team over the past decade. The categorization was utilized to organize the regression analysis data into four distinct and actionable levels depending on the RMS readings of the defective bearing component.

Table 4. Catalogued condition parameters using RMS values

Average Defect Area [cm^2]		**RMS Value [g]**	**Condition /Indication**	**Residual Mileage [km] / [mi]**
Cup	**Cone**			
4	3	<8	Good / Green	> 80k / 50k
13	9	8 – 17	Monitor / Yellow	40k – 80k / 25k – 50k
35	28	17 – 25	Warn / Orange	16k – 40k / 10k – 25k
58	38	> 25	Act / Red	< 16k / 10k

While the condition parameters in Table 4 apply to both inner (cone) and outer (cup) rings, it is important to note that the average defect area corresponding to the RMS ranges selected will vary for each component. While a "monitor condition" (yellow indication) is triggered by cups with an average defect size of13 cm^2, cones will reach that same condition at an average spall area of 9 cm^2. The disparity in the average defect area between these two bearing components increases with the RMS values. For an RMS value of eight or less, the average defect areas of the cone and cup components have a difference of only 1 cm^2, which increases to 20 cm^2 by the time the RMS values correspond to a red indication (RMS > 25).

The average defect area variation in cup and cone components coincide with that seen in the spall area thresholds of Figure 19 and Figure 20. The threshold observed in the cone spall area versus mileage regression analysis shows that an inner ring spall will have an accelerated deterioration trend at a defect area lower than that of an outer ring. The accelerated propagation rate threshold in cones can explain the higher RMS values observed at smaller defect sizes considering that a more rapid deterioration will generate increased vibration levels within he bearing. Another reason for the smaller defect size in inner rings is the components motion behavior. The bearing outer ring is a static component while the inner ring rotates with the axle.

While both elements experience the rollers rotating and rolling along the raceway, the cyclic cone rotation in and out of the loaded zone creates a higher defect frequency (ω_{cone}=167.8 Hz) than that seen in a stationary cup (ω_{cup}=135.6 Hz) at a simulated train traveling velocity of 137 km/h (85 mph).Cone rotation will also result in slower spall progression. Due to their cyclic loading, bearing inner rings do not experience as many load cycles per rotation as do the outer rings. They will see one full load cycle per rotation while an outer ring spall will see 23 full cycles in that same rotation and thus cone spalls will take longer to reach larger sizes. As a result of this slower growth, cone spalls larger than 15 cm^2 are uncommon and difficult to generate in the laboratory.

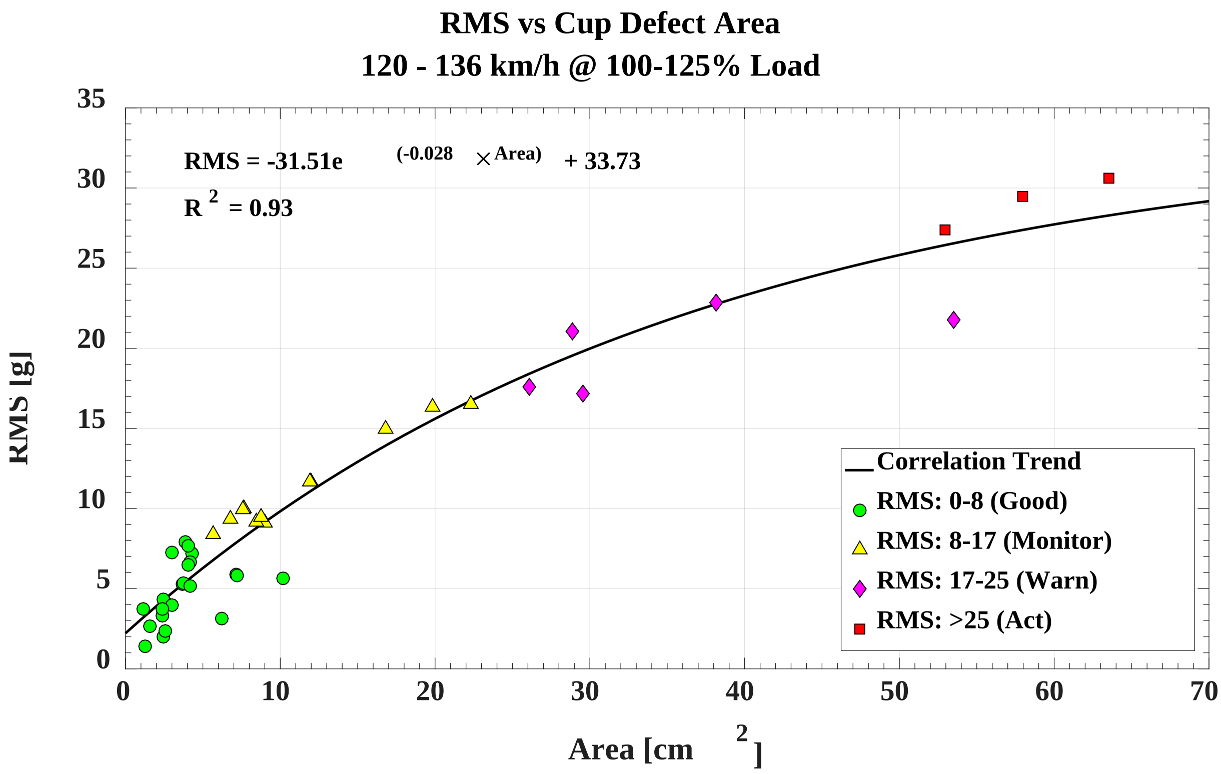

Figure 24. RMS vs cup spall area regression model with condition parameters

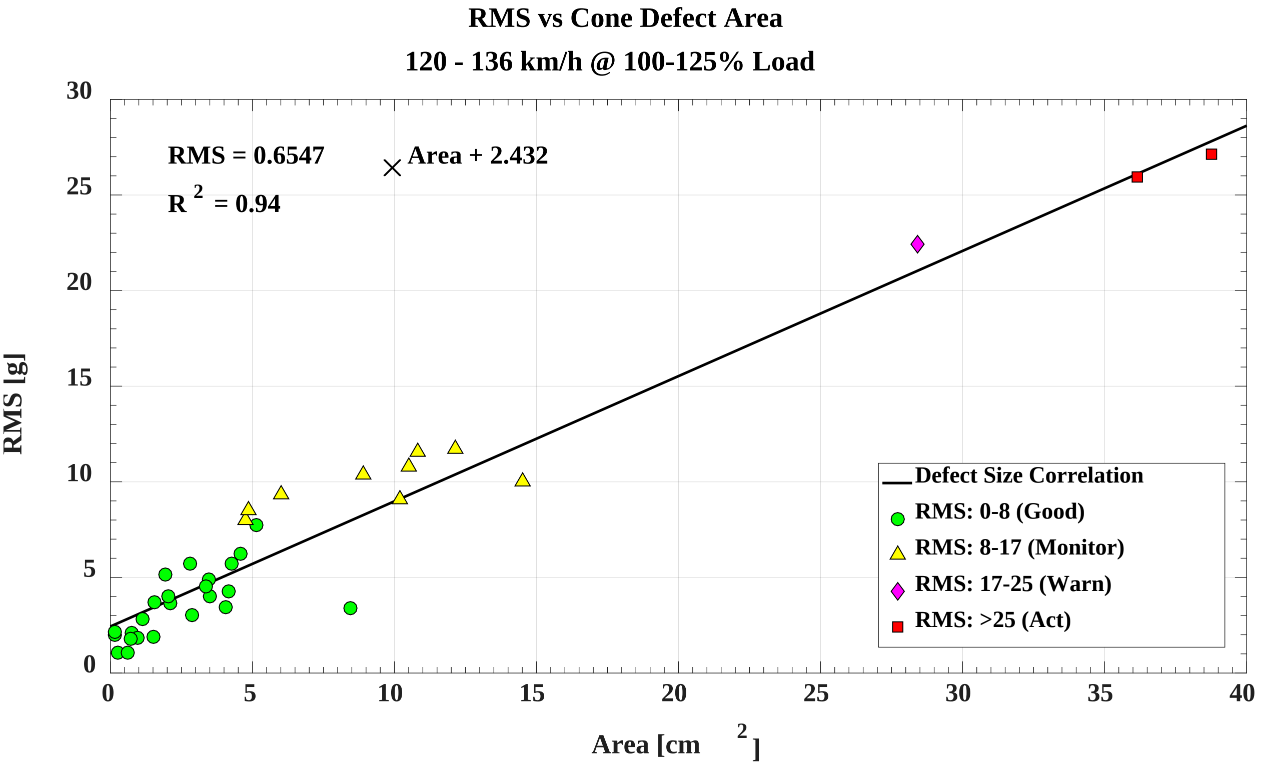

Figure 25.RMS vs cone spall area regression model with condition parameters

4.2 Spall Growth Rate Patterns

The distance traveled for each experiment was recorded and used to calculate the component spall area growth rate. Figure 26 and Figure 27 shows the area growth rate versus the defect size (area) for cups and cones, respectively. Two trends emerged in both the outer ring (cup) and inner ring (cone) data acquired, namely: an upper bound growth rate correlation (GR1) and a lower bound growth rate correlation (GR2). The reason behind the two distinct growth rate trends is the presence and location of the subsurface inclusions in each raceway. For example, a raceway with several clustered subsurface inclusions near the surface of the raceway will have defects develop at a faster rate as opposed to a raceway with fewer or more dispersed subsurface inclusions. The GR1 equation is used to provide a worst-case scenario for estimating the residual life of a defective bearing assuming the presence of multiple subsurface inclusions. While GR2 is a lower bound equation that provides a baseline growth rate for its respective component.

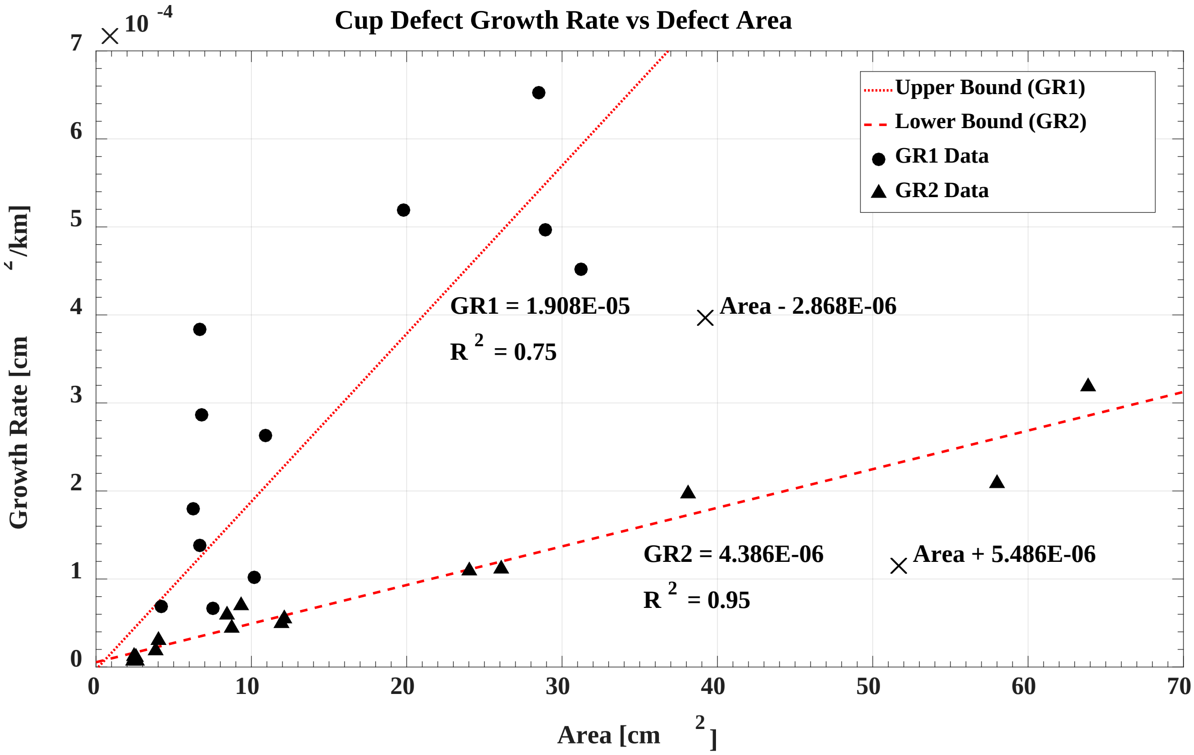

Figure 26. Cup spall area growth rate versus cup spall area

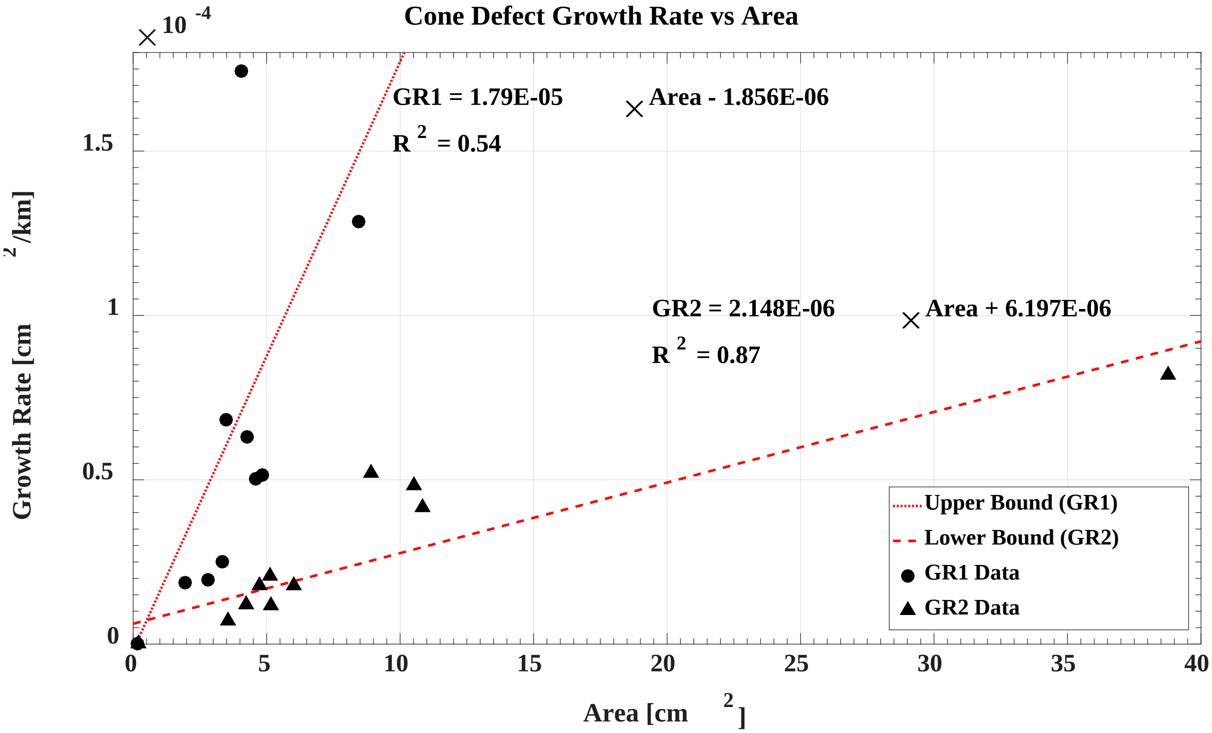

Figure 27. Cone spall area growth rate versus cone spall area

Examining the growth rate models, one can notice that the goodness-of-fit R^2 value for both the inner and outer rings GR1 trendline is lower than that for the GR2. The scatter in the GR1 data points can be attributed to the variation in quantity and location of the material's subsurface inclusions. Location of subsurface inclusions is significant both in terms of depth and in proximity to other subsurface inclusion. Material impurities conglomerated in a single area are likely to group and create an accelerated growth rate.

A correlation between RMS and defect growth rate was developed by combining the relations provided by the RMS versus defect area and the defect growth rate versus defect area regression analysis models. The defect area parameter in the growth rate trend was equated to the area variable in its respective component RMS regression fit. As a result, the RMS versus defect growth rate correlations for cups and cones, presented in Figure 28 and Figure 29, respectively, were devised. The upper bound (GR1) and lower bound (GR2) in these models encompass the possible ranges for the defect growth rate values acquired from the associated RMS values.

The cup (outer ring) trendlines seen in Figure 28 exhibit natural logarithmic (ln) behavior due to the exponential function found in the RMS versus defect area regression model. The possible range of growth rates defined by the GR1 and GR2 boundaries is initially limited and increases with the RMS as the exponential trendlines diverge from each other. Since RMS increases as the defect area grows larger (seen in Figure 22 and Figure 23), it is clear that larger defects have a margin of uncertainty in growth rate. Figure 29 presents the GR1 and GR2 trendlines for the cone (inner ring). Note that, unlike the cup trendlines, the upper (GR1) and lower (GR2) growth rate trendlines for the cone exhibit a linear function as is the case for the cone correlations seen in the RMS versus defect area plot (Figure 23).

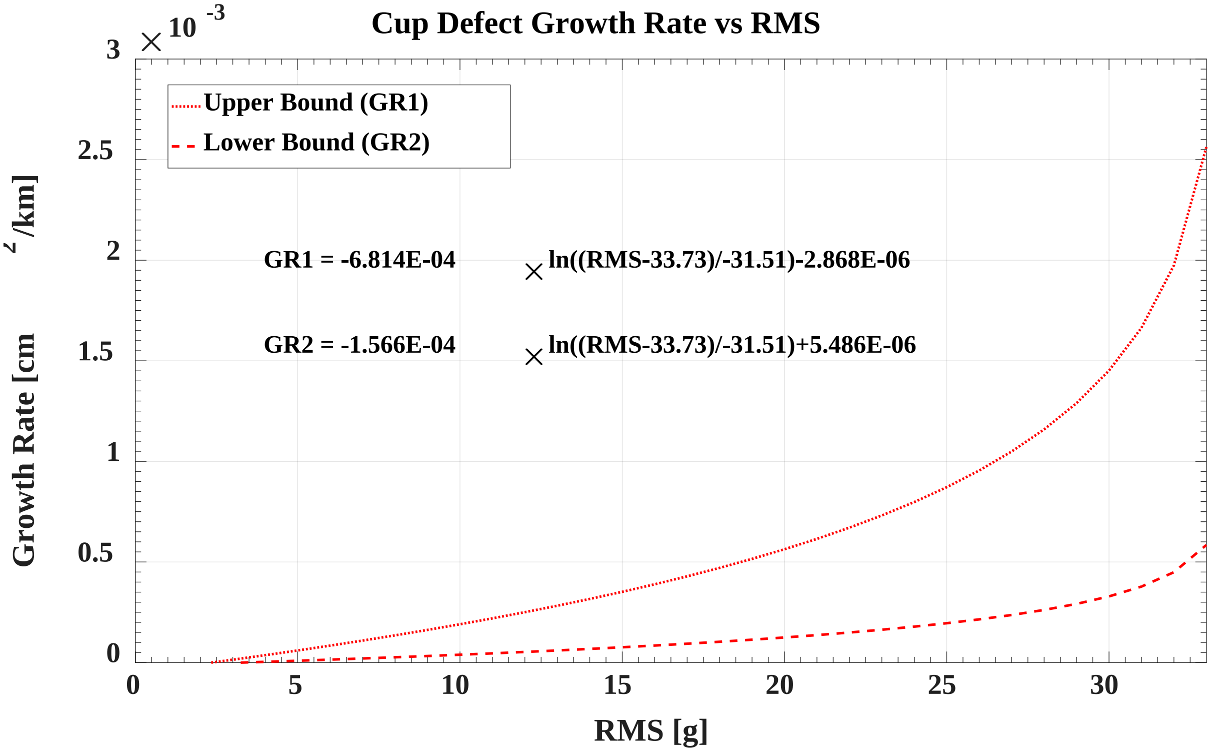

Figure 28. Cup spall area growth rate versus RMS

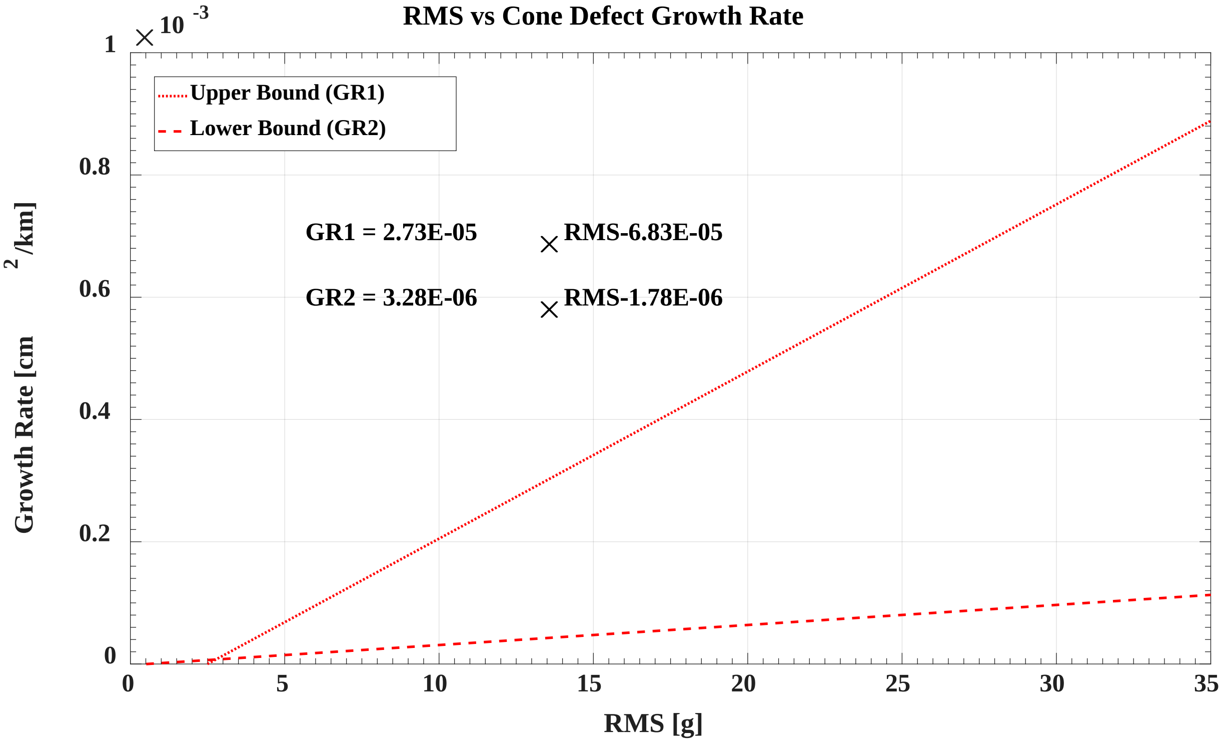

Figure 29. Cone spall area growth rate versus RMS

4.3 Laboratory Experiment

4.3.1 Laboratory Experiment 200: Cup Defect

Experiment 200 featured an outer ring (cup) with an initially pitted inboard raceway, shown in Figure 30(left). The cup ran on the four-bearing tester (4BT), placing the pitted area in the maximum load position to simulate a worst-case scenario. The experiment ran a total of 81,600 km (50,700 miles) during which the pitted raceway developed a spall with an area of 9 cm^2 (1.4 in^2), pictured in Figure 30 (right). The resulting defect area corresponds to approximately 2.5% of the total area (367 cm^2) of a class K or class F outer ring raceway.

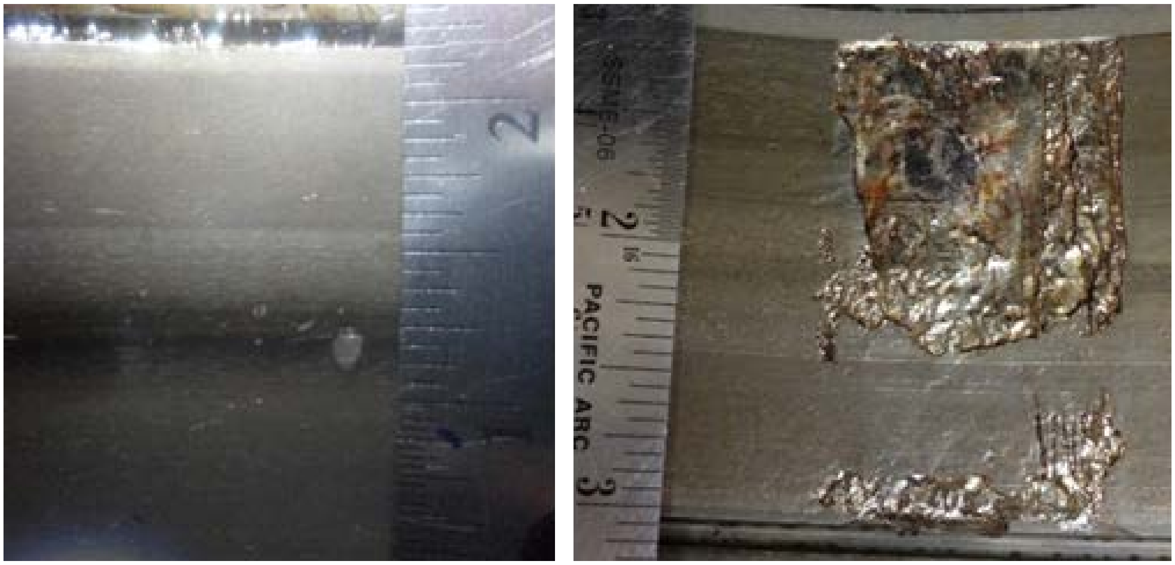

Figure 30. Experiment 200: Initial cup raceway (left) and final cup raceway (right)

Figure 31 shows the vibration and temperature profiles for Bearing 2 (B2) (refer to Figure 11. Top view of four-bearing tester (4BT) during Experiment 200, in which the bearings were operated at full speed (137 km/h or 85 mph) and 110% of full load conditions. The bearing was pulled out once it was deemed defective by the condition monitoring algorithm. The maximum threshold (denoted by the solid red line) in the vibration and temperature profiles represents the highest value a healthy bearing will display under the given operating conditions. Therefore, any bearing operating with a signature above the maximum RMS threshold is expected to be defective and removed from the test axle and disassembled in order to be inspected for defect propagation.

Averaging the last two hours of the SA accelerometer, an RMS of 9 g was found. The RMS was used to calculate a theoretical defect area using the equation found in the outer ring RMS versus defect area regression analysis (Figure 24). The calculated defect area of 8.8 cm2, listed inTable 6, is 98% of the actual area (i.e., a 2% error). The RMS value was also used to calculate the upper and lower growth rate boundaries for the defective outer ring. Using the GR1 and GR2 equations from the growth rate versus RMS plot the upper and lower bounds yielded values of 1.7E-04 cm2/km and 0.4E-04cm2/km, respectively. The actual growth rate, as measured during the visual inspection, was 1.0E-04cm2/km which falls well within the range provided by the regression analysis, as can be observed in Figure 32.

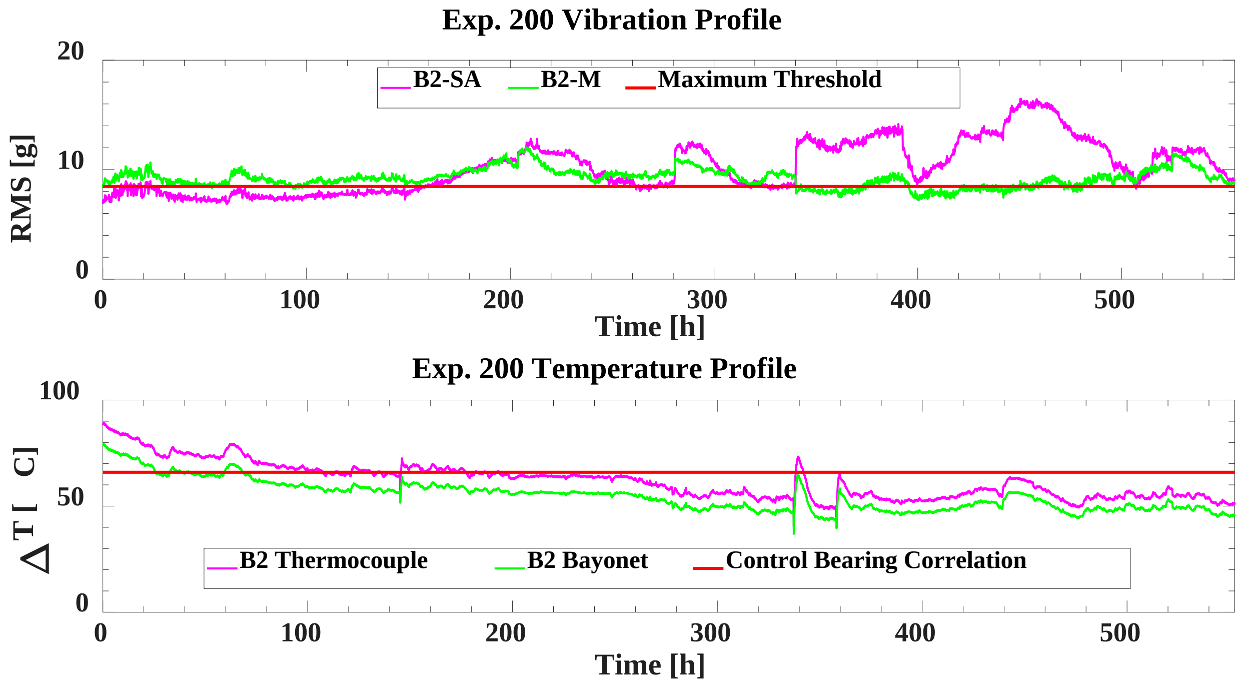

Figure 31. Vibration and temperature profiles for Experiment 200

Table 5. Average values for the final two hours of Experiment 200 (ambient temperature during the experiment was 23°C or 73°F)

Experiment 200 (Bearing 2 Cup Spall)			
Track Speed [km/h]/[mph]	Load [%]	Temperature above Ambient (ΔT) [°C / °F]	RMS [g]
137/85	110	48/87	9

Table 6. Spall size and spall growth rate values for Experiment 200

RMS	**Defect Size [cm^2]/[in^2]**	**Calculated Defect Size [cm^2]**	**Percent Error [%]**
9	9/1.4	8.80	2
	Lower Bound Growth Rate [cm^2 / km] × 10^{-4}	**Actual Growth Rate [cm^2 / km] × 10^{-4}**	**Upper Bound Growth Rate [cm^2 / km] × 10^{-4}**
	0.4	1.0	1.7

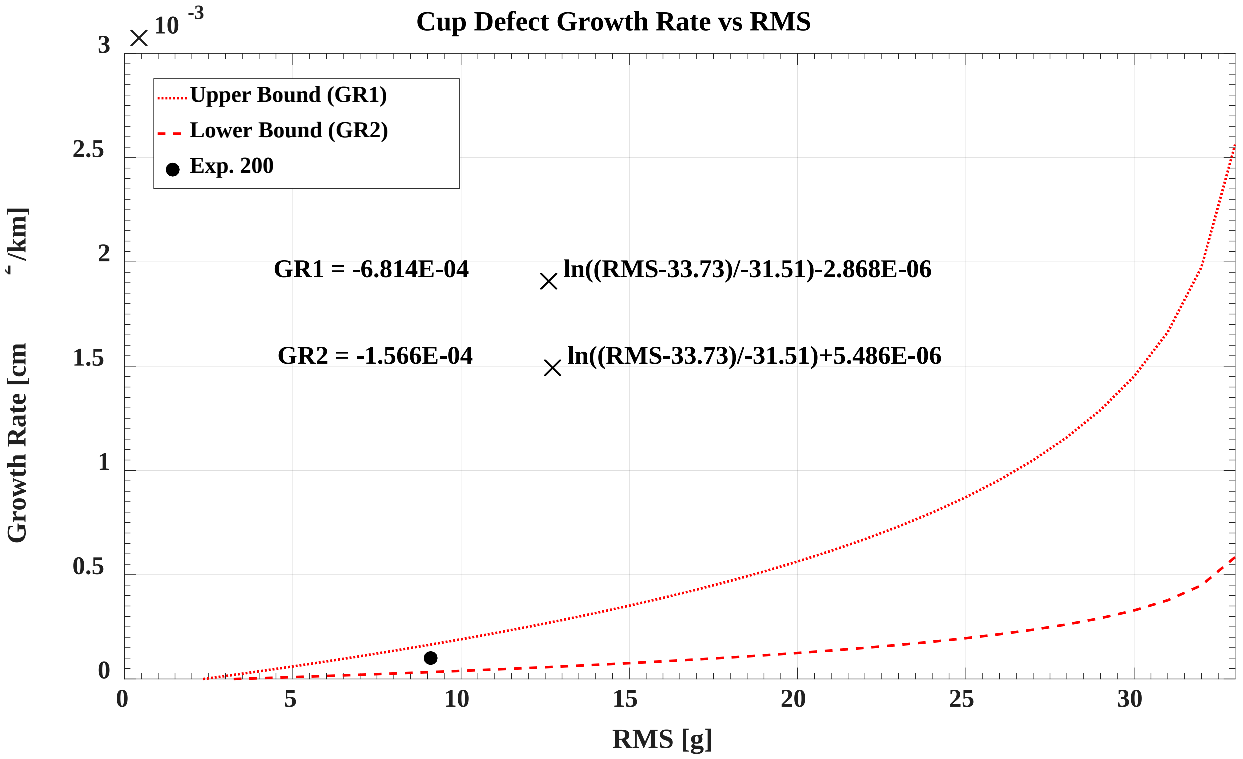

Figure 32. Experiment 200 cup spall growth rate in relation to the developed regression model

The average spall size corresponding to an outer ring (cup) red indication (i.e., act condition) is 58 cm^2, which accounts for 16% of the total 367 cm^2 area for a single class K or class F outer ring raceway. If the upper bound growth rate of 1.7E-04 cm^2/km is used to simulate a worst-case defect propagation scenario, it will take approximately 288,000 km (179,000 mi) for the spall to grow to a size where action will be needed (red indication). This residual life prognostic affords rail operators plenty of time to develop a proactive maintenance schedule which will minimize costly and premature maintenance stoppages and delays.

4.3.2 Laboratory Experiment 184B: Cup Defect

An outer ring (cup) with an initial inboard spall area of 24 cm^2 (3.7 in^2), which had a previous RMS vibration value of 16 g (monitor condition/yellow indication), was placed in the B3 location (refer to Figure 11) of the four-bearing tester (4BT) for further defect propagation. Like Experiment 200, Experiment 184B had the defect location positioned directly in the region of maximum applied load. After running a simulated distance traveled of 47,000 km (29,000 mi) at full speed and full load conditions, the defect area grew to a size of 53 cm^2 (8.2 in^2), as depicted in Figure 33 (right). The post experiment defect warranted a red indication (act condition) due to its vibration signature giving an RMS of 27 g while encompassing 14% of one outer ring raceway area (367 cm^2).

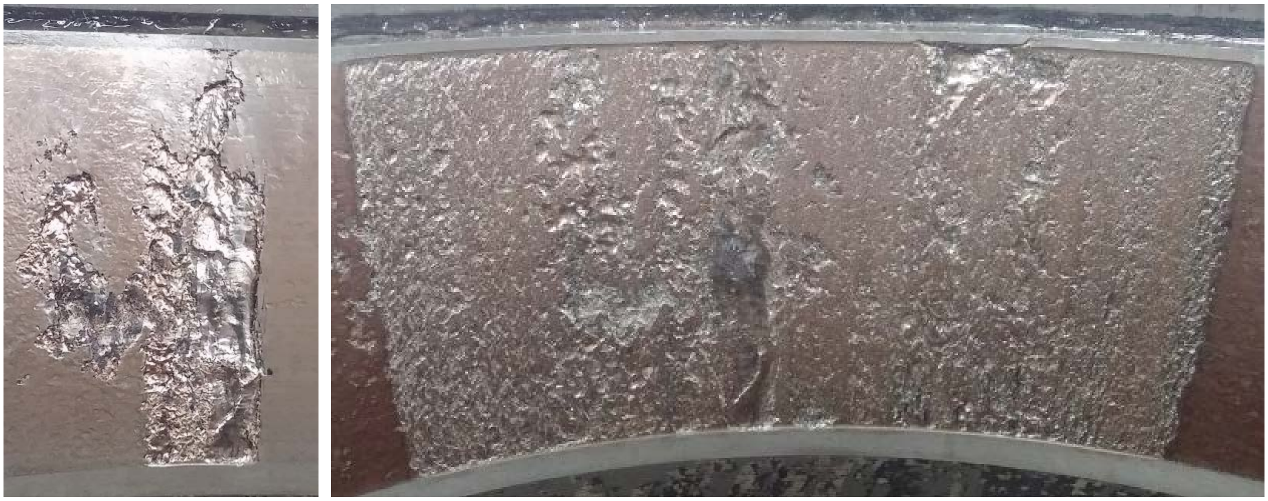

Figure 33. Experiment 184B: Initial cup raceway (left) and final cup raceway (right)

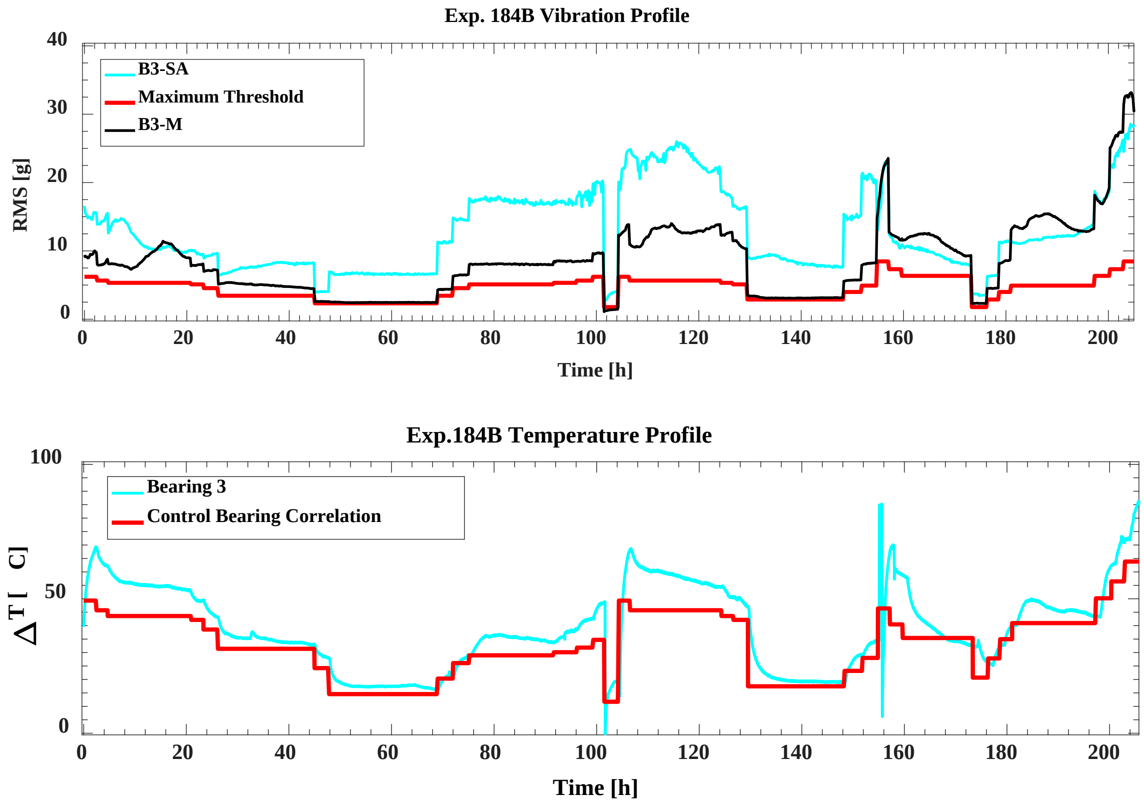

Figure 34. Vibration and temperature profiles for Experiment 184B

Using the RMS value of 27 g, a defect area of 55 cm^2 was calculated utilizing the model provided in Figure 24. Hence, the model predicted the defect size with an error of only 4%. The upper and lower growth rate bounds calculated through the RMS yielded values of 10.9E-04 cm^2/km and 0.3E-04 cm^2/km, respectively. The actual growth rate of 6.1E-04cm^2/km falls well within the margin formed by these two boundaries, as can be seen in Figure 35.

Table 7. Average values for the final two hours of Experiment 184B (ambient temperature during the experiment was 23°C or 73°F)

Experiment 184B (Bearing 2 Cup Spall)			
Track Speed [km/h]/[mph]	Load [%]	Temperature above Ambient (ΔT) [°C / °F]	RMS [g]
137/85	100	86/187	27

Table 8. Spall size and spall growth rate values for Experiment 184B

RMS	**Defect Size [cm^2] /[in^2]**	**Calculated Defect Size [cm^2]**	**Percent Error [%]**
27	53/8.2	55	4
	Lower Bound Growth Rate [cm^2 / km] × 10^{-4}	**Actual Growth Rate [cm^2 / km] × 10^{-4}**	**Upper Bound Growth Rate [cm^2 / km] × 10^{-4}**
	0.3	6.1	10.9

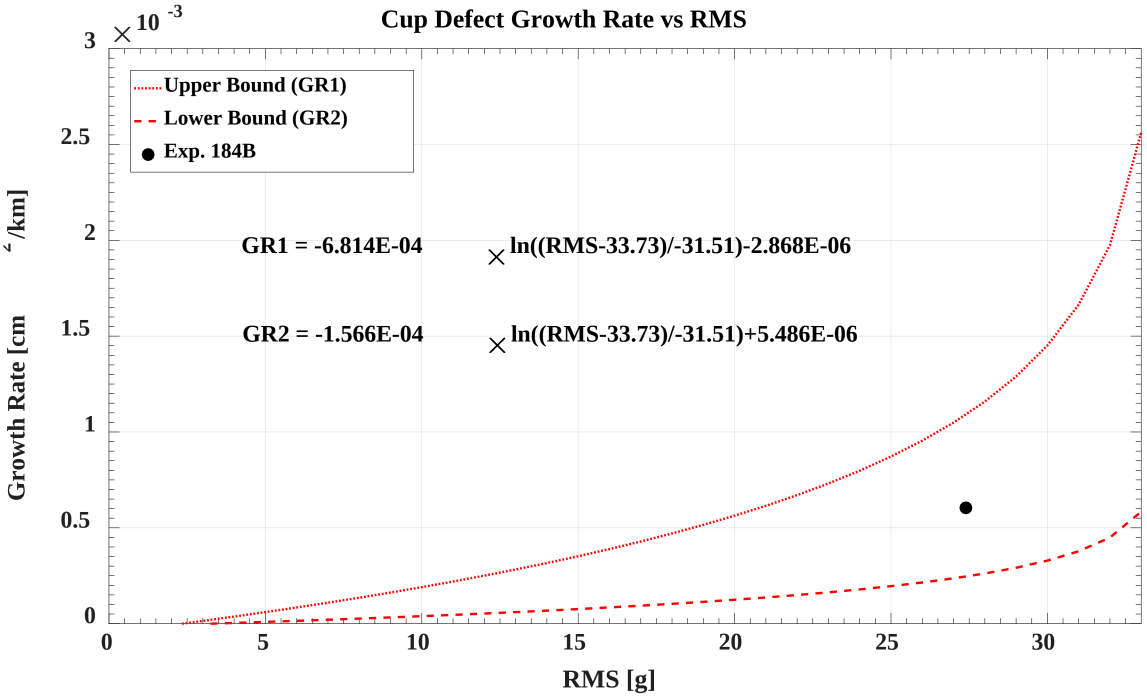

Figure 35. Experiment 184B cup spall growth rate in relation to the developed regression model

Since the initial cup defect yielded an RMS value of 16 g in Experiment 184A, it was categorized as a yellow indication (monitor condition). Referring Table 4, the residual life of a spall categorized within an 8 - 17 g RMS value has a range of 40,000 - 80,000 km (25,000 - 50,000 miles). Experiment 184B lies within this residual life estimate, taking a total of 47,000 km (29,000 mi) for a yellow indication to reach its service life (red indication)

4.3.3 Laboratory Experiment 202A: Cone Defect

In Experiment 202A, a defective cone with an initial spall area of 9 cm^2 (1.4 in^2) was placed in the single-bearing tester (SBT) for further defect propagation. The experiment ran under full-speed (137 km/h) and full load conditions (100% load) for a total of 33,000 km (20,500 mi) during which the spall size grew to 10.5 cm^2 (1.6 in^2). Figure 37 shows the vibration (top) and temperature (bottom) profiles for the duration of this experiment.

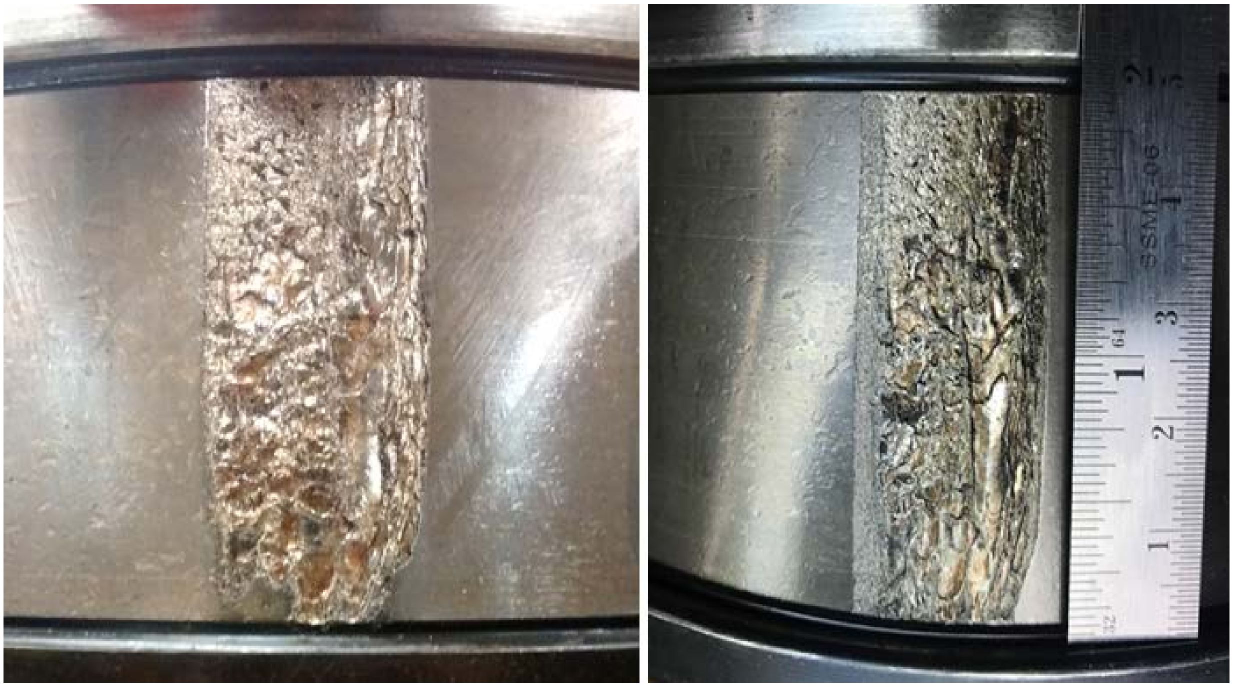

Figure 36. Experiment 202A: Initial cone raceway (left) and final cone raceway (right)

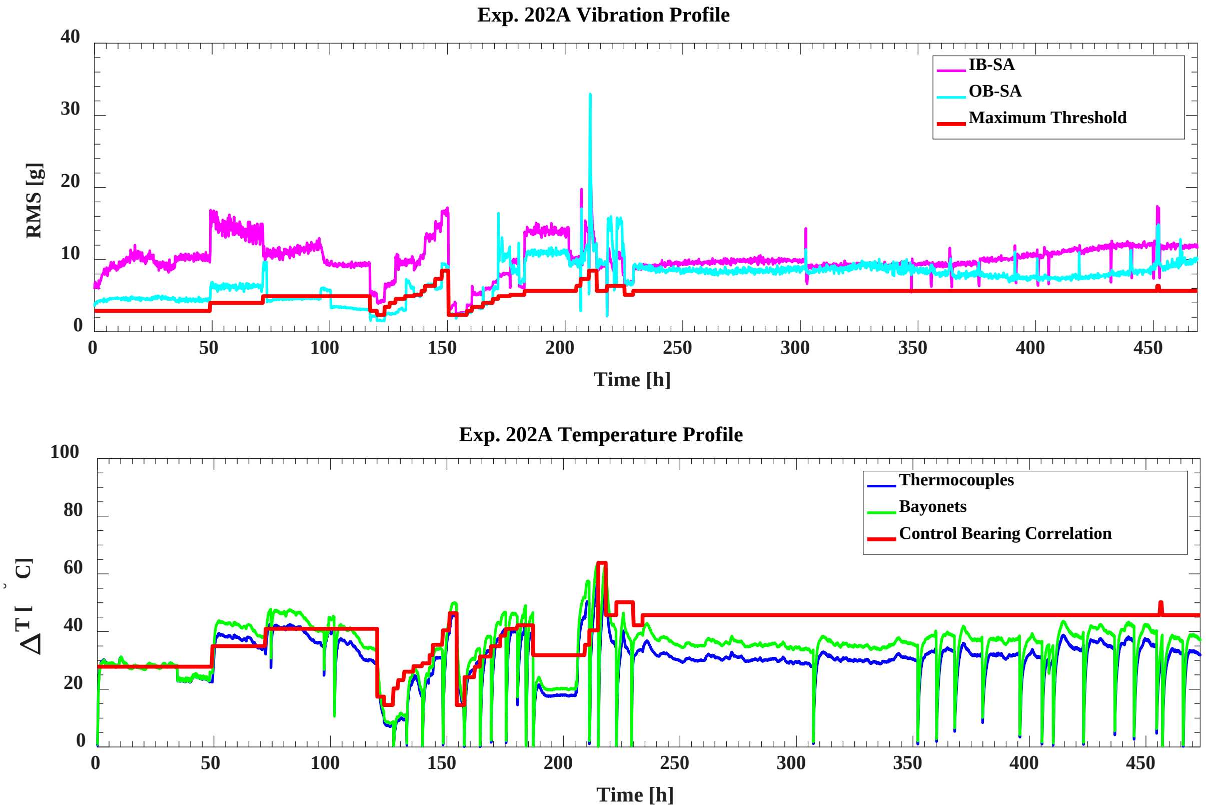

Figure 37. Vibration and temperature profiles for Experiment 202A

An RMS value of 11 g was obtained after taking the average of the last two experiment hours for both the inboard (IB) and outboard (OB) SmartAdapter^{TM} (SA) locations. This RMS (root-mean-square) value was used to calculate a 13 cm^2 defect area, which is off by about 24% as compared to the actual spall size. The shortage of data containing inner ring spall areas above 6.5 cm^2 (1 in^2) can account for the lower confidence in the calculated cone defect size when compared to the outer ring examples provided by Experiment 200 and Experiment 184B. When calculating the upper and lower bound growth rates, values of 2.3E-04 cm^2/km and 0.3E-04 cm^2/km were obtained, respectively. Therefore, while the accuracy of the theoretical defect area decreased, the RMS versus defect area growth rate regression analysis still proves functional. Figure 38 displays the defect growth rate for Experiment 202A which falls within the margin dictated by the growth rate boundaries formed through the regression analysis.

Table 9. Average values for the final two hours of Experiment 202A
(ambient temperature during the experiment was 23°C or 73°F)

Experiment 202A (Bearing Cone Spall)			
Track Speed [km/h]/[mph]	Load [%]	Temperature above Ambient (ΔT) [°C / °F]	RMS [g]
137/85	100	28/83	11

Table 10. Spall size and spall growth rate values for Experiment 202A

RMS	**Defect Size $[cm^2]$ /$[in^2]$**	**Calculated Defect Size $[cm^2]$**	**Percent Error [%]**
11	10.5/1.6	13	24
	Lower Bound Growth Rate $[cm^2 / km] \times 10^{-4}$	**Actual Growth Rate $[cm^2 / km] \times 10^{-4}$**	**Upper Bound Growth Rate $[cm^2 / km] \times 10^{-4}$**
	0.3	0.5	2.3

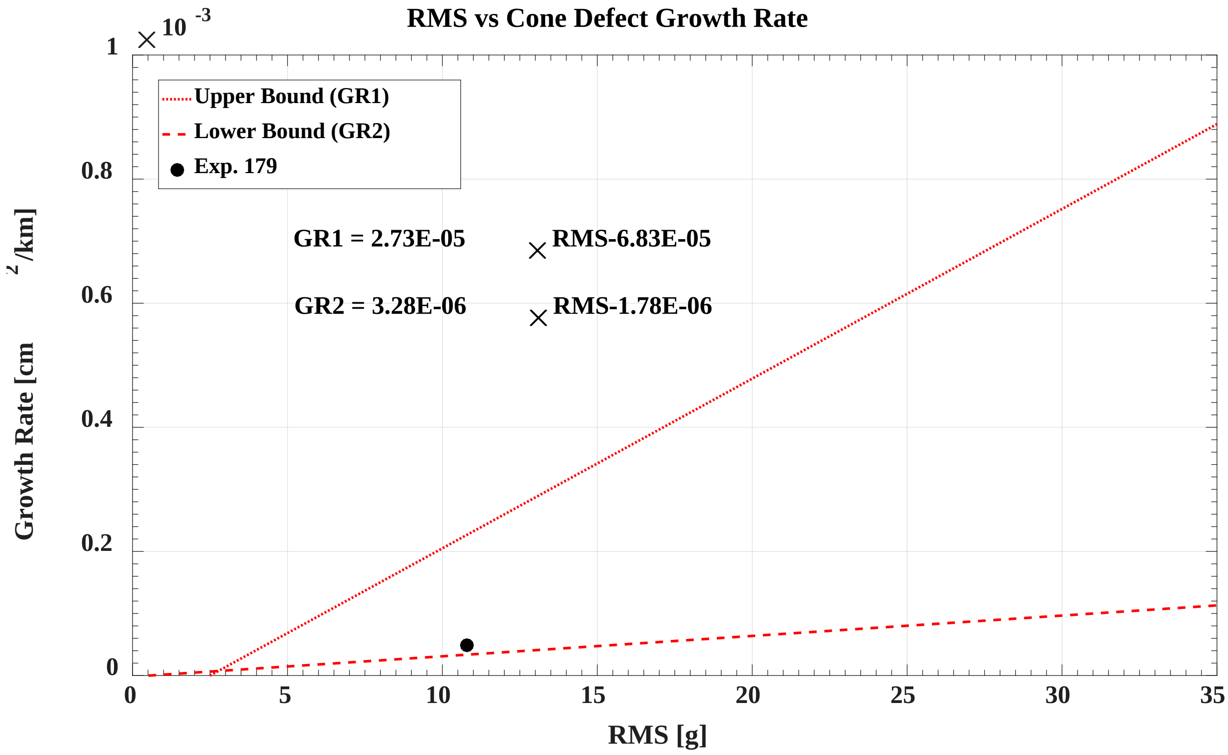

Figure 38. Experiment 202A cone spall growth rate in relation to the developed regression model

Although the defect growth rate for Experiment 202A falls closer to the lower bound trendline, the upper bound defect growth rate was still used to predict a worst-case scenario. Using the upper bound growth rate of 2.3E-04 cm^2/km, it would take approximately 119,500 km (74,000 mi) for the defect to reach about 14% of the total inner ring raceway surface area (279 cm^2) and signal a red indication (i.e., act condition) alert.

4.3.4 Laboratory Experiment 206: Cone Defect

Previously, it was mentioned that cone defects with areas larger than 6.5 cm^2 (1 in^2) were scarce due to the cyclic motion of the component. Therefore, in order to facilitate and ensure thorough defect progression tracking, components with large defect areas are run in the single-bearing tester (SBT) which allows for easier and faster mounting and removal of the test bearing. Experiment 206 consisted of an inner ring with multiple defects containing a total spall area of 36 cm^2 (5.6 in^2), pictured in Figure 39. The experiment performed on this component prior to Experiment 206 gave a vibration signature (RMS) of 26 g, categorizing the inner ring as an act condition component (red indication).

Experiment 206 operated at full speed and full load conditions on the SBT for a simulated distance traveled of 14,000 km (9,000 mi) in which the spall area increased to 39 cm^2 (6 in^2), as shown in Figure 40. The experiment was stopped, and the bearing was disassembled and visually inspected once the vibration signatures indicated further propagation of the spall had occurred. Propagation patterns can be observed in Figure 41 (top) starting from experiment hour 100.

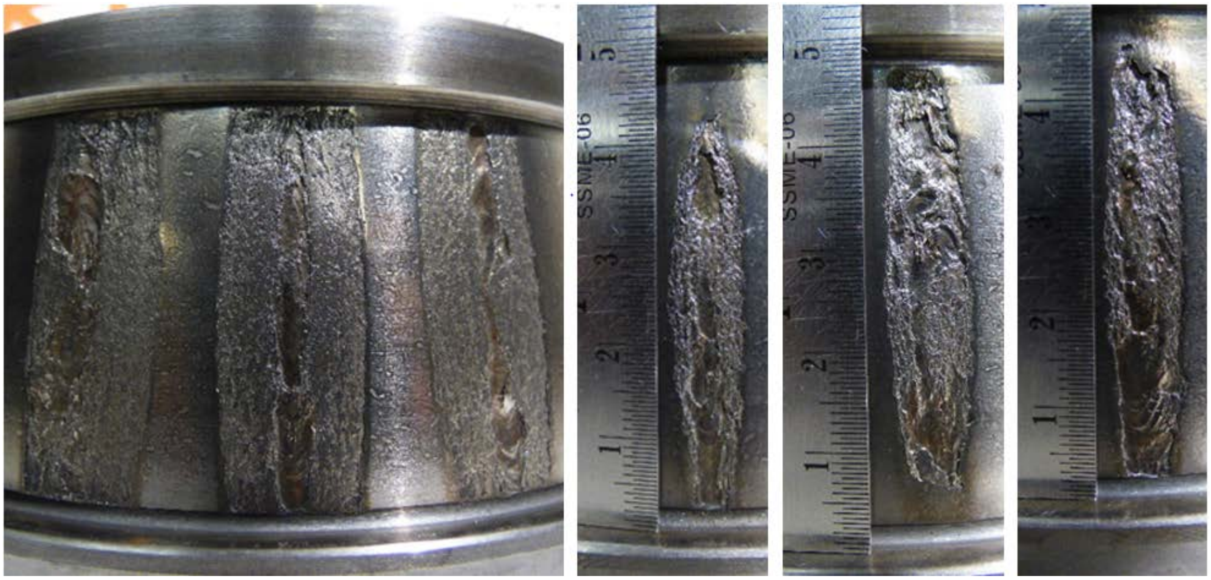
SSME-06
SSME-06

Figure 39. Experiment 206 initial cone raceway (multiple spalls)

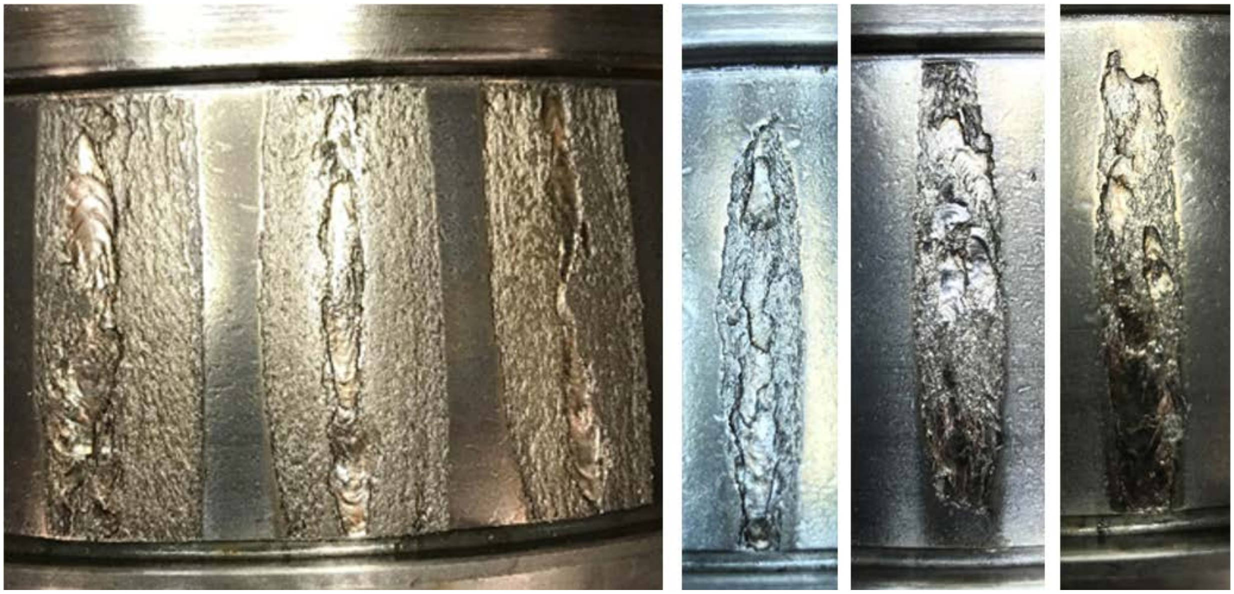

Figure 40. Experiment 206 final cone raceway

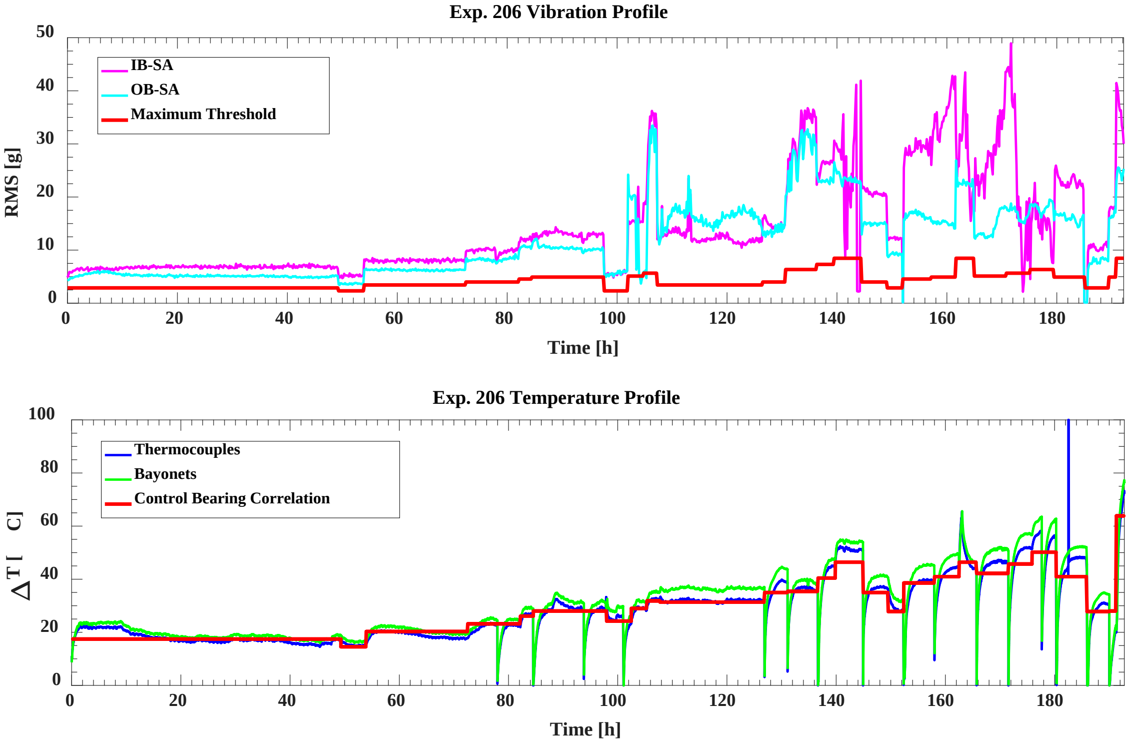

Figure 41. Vibration and temperature profiles for Experiment 206

The inboard (IB) and outboard (OB) SmartAdapter^{TM} vibration signatures were averaged for the last two hours of the experiment, giving an RMS value of 26.5 g. The RMS value obtained was used to calculate the theoretical defect area as well as the upper and lower bound growth rates which are listed in Table 11 and Table 12, respectively. The calculated defect size of 37 cm^2 has only a 5% error as compared to the actual spall area. The higher accuracy in Experiment 206 compared to the inner ring in Experiment 202A can be attributed to the previously explained higher fidelity fit for growth of spalls with areas above 6.5 cm^2 (1 in^2), as compared to those with areas below that threshold, as shown in Figure 19 (y2).

The actual growth rate was calculated using the total distance traveled during the experiment, yielding a value of 1.8E-04cm^2/km. The upper and lower growth rate bounds were calculated for an RMS of 26.5 g and resulted in 6.5E-04cm^2/km and 0.9E-04 cm^2/km, respectively. Figure 42 shows the actual growth rate of Experiment 206 in relation to the growth rate versus RMS regression models. It can be observed that this data point falls within the growth rate margins projected.

Table 11. Average values for the final two hours of Experiment 206
(ambient temperature during the experiment was 23°C or 73°F)

Experiment 206 (Bearing Cone Spall)			
Track Speed [km/h]/[mph]	Load [%]	Temperature above Ambient (ΔT) [°C / °F]	RMS [g]
137/85	100	68/155	26.5

Table 12. Spall size and spall growth rate values for Experiment 206

RMS	**Defect Size [cm^2] /[in^2]**	**Calculated Defect Size [cm^2]**	**Percent Error [%]**
27	39/6	37	5
	Lower Bound Growth Rate [cm^2 / km] × 10^{-4}	**Actual Growth Rate [cm^2 / km] × 10^{-4}**	**Upper Bound Growth Rate [cm^2 / km] × 10^{-4}**
	0.9	1.8	6.5

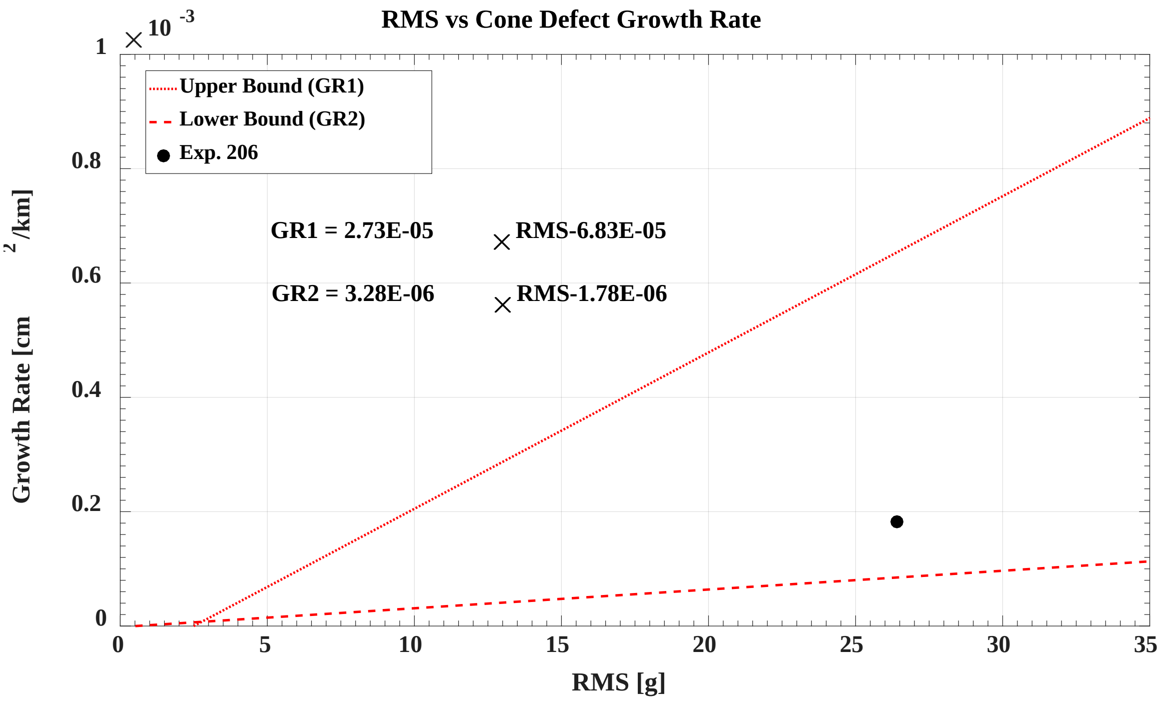

Figure 42. Experiment 206 cone spall growth rate in relation to the developed regression model

As previously mentioned, the component used for Experiment 206 had a pre-test RMS value of 26 g causing it to be in an act condition (red indication) with a predicted residual service life of less than 16,000 km (10,000 miles). Experiment 206 was only able to run 14,000 km (9,000 mi) before it was necessary to stop this test to avoid a catastrophic bearing failure. The results from Experiment 206 further support the accuracy and reliability of the residual life prognostic models developed in this study.

Finally, comparing the cup and cone laboratory experiment examples, it is clear that the cone defect growth rates fall closer to the lower bound growth rate trend (GR2) while the outer ring (cup) defect growth rates rest along the center between the two boundaries. This pattern can again be explained by the loading conditions of the tapered roller bearing components. The outer ring (cup) is a static component which keeps a standard load applied while the cone experiences cyclic loading as it rotates with the axle. The cyclic loading in the cone causes slower defect propagation as it doesn’t experience the same constant stresses as the outer ring (cup).

CHAPTER V

CONCLUSIONS

Train derailments are a significant and widely recognized problem for both environmental and monetary resources in the railroad industry. However, unnecessary stoppages and in-service failures (ISFs) can account for a large portion of the financial waste by creating delays and needless premature maintenance expenditures. These problems are primarily rooted in the bearing health condition monitoring systems currently used in the field. The TADS^{TM} and HBDs wayside condition monitoring systems which, while scarcely found in the field, are the most commonly used in the railroad industry. These detectors are specialized in finding end-of-life bearings prone to causing train derailments but remain ineffective at minimizing ISFs.

The University Transportation Center for Railway Safety (UTCRS) developed SmartAdapter^{TM} in order to provide an effective onboard system for the continuous monitoring of the bearing temperature and vibration profiles. This onboard data acquisition tool works in conjunction with a defect detection algorithm which provides real-time information on defect existence, component location, and approximate size. Defect detection is accomplished through the vibration profile provided by this onboard bearing health monitoring system and has been crucial in developing the residual life prognostic models presented in this thesis.

After further population of the RMS versus defect area models previously developed, the regression analysis was used together with the components growth rate patterns to form relative growth rate boundaries. The growth rate range for a component can be found through the vibration signature of the bearing. Once the RMS values are provided by the onboard condition monitoring system, the prognostic models will calculate worst-case and best-case scenario growth rates for the component in question.

The laboratory experiments provided as examples in Chapter 4 attest to the accuracy of the residual life prognostic models developed. The enhanced RMS versus defect area regression analysis can calculate the component defect area with reliable precision. The same RMS value used to obtain a defect size estimate can then be utilized to form a growth rate boundary for the spalled component. The RMS versus defect growth rate models display an initially narrow growth rate boundary which allows for stringent growth rate estimates in spalls with smaller defect areas. However, as seen on example Experiments 184B and 206, larger spall areas conform well within the residual life condition parameters displayed in Table 4. Therefore, while the boundaries in the RMS versus defect growth rate regression analysis might allow for a greater variance when estimating larger defect size growth rate patterns, it was proven that the catalogued condition parameters provide accurate residual life assessments.

Further data acquisition will be useful to continue to populate the regression analysis models used, thus, increasing the accuracy of the residual life estimates. Data points for larger defect sizes, particularly for inner ring (cone) components, will help increase the precision in calculating defect size estimates and minimize the divergence between the upper bound and lower bound growth rate curves seen in the RMS versus defect growth rate models.

A proper maintenance schedule for railcar bearings will decrease not only derailments, but also in-service failures (ISFs) and premature maintenance costs. Current bearing health monitoring technologies such as TADS^{TM} only detect end-of-life bearings (with defect areas over 90% of the component raceway) which call for immediate action often creating ISFs. The vibration parameters developed for bearing residual life will enable an act condition (red indication) in bearing defects covering 15% of the component raceway and allow up to 16,000 km (10,000 mi) for appropriate maintenance procedures to be implemented, thus, preventing ISFs.

With the regression analysis presented for the inner ring (cone) and outer ring (cup) components, a proactive maintenance schedule can be developed, consequently minimizing the occurrence of derailments as well as ISFs and premature maintenance. These residual life models work in conjunction with the SmartAdapter™ technology developed by the UTCRS research team. Constant monitoring of the bearing’s vibration profiles will allow the detection of the onset of defect initiation, and proper residual life estimates can be provided through the regression analysis models presented in this thesis. The catalogued condition parameters presented in Table 4 also serve as an overview of the residual life of a component.

REFERENCES

[1] Liu, Xiang, M. RapikSaat, and Christopher PL Barkan. "Analysis of causes of major train derailment and their effect on accident rates." Transportation Research Record 2289.1 (2012): 154-163.

[2] https://www.schaeffler.my/remotemedien/media/_shared_media/08_media_library/01_publications/schaeffler_2/brochure/downloads_1/pbs_de_en.pdf

[3] Office of Safety Analysis, FRA, U.S. Department of Transportation. Sec. 3.01–3.04, 9.01, and 9.05. http://safetydata.fra.dot.gov/officeofsafety/. Accessed Jan. 30, 2020.

[4] Schlake, Bryan W., Christopher PL Barkan, and J. Riley Edwards. "Train delay and economic impact of in-service failures of railroad rolling stock." Transportation research record 2261.1 (2011): 124-133.

[5] Anderson, Gerald B. "Acoustic detection of distressed freight car roller bearings." ASME/IEEE 2007 Joint Rail Conference and Internal Combustion Engine Division Spring Technical Conference. American Society of Mechanical Engineers Digital Collection, 2007.

[6] An Implementation Guide for Wayside Detector Systems. (n.d.). Retrieved January 30, 2020, from http://www.trb.org/Main/Blurbs/179225.aspx

[7] Southern, Carolyne, David Rennison, and Uwe Kopke. "RailBAM-An advanced bearing acoustic monitor: initial operational performance results." CORE 2004: New Horizons for Rail (2004): 23.

[8] Ose, Mixanikos. "Heat Detectors-box and Brake Disc (Hot Box & Hot Wheel Detection System)." *Heat Detectors-box and Brake Disc (Hot Box & Hot Wheel Detection System)*. N.p., 16 July 2015. Web.

[9] A. Mealer, C. Tarawneh, S. Crown, Radiative Heat Transfer Analysis of Railroad Bearings for Wayside Hot-box Detector Optimization. *Proceedings of the 2017 Joint Rail Conference*, Philadelphia, PA, April 4-7, 2017.

[10] J. Aranda, “Radiative Heat Transfer Analysis of Railroad Bearings for Wayside Thermal Detector Optimization,” Master's Thesis, Department of Mechanical Engineering, The University of Texas Rio Grande Valley, December 2018.

[11] C. Tarawneh, J. Aranda, V. Hernandez, S. Crown and J. Montalvo. "An investigation into wayside hot-box detector efficacy and Optimization," *International Journal of Rail Transportation*, under review, submitted March 2019.

[12] J. G. Tabbachi, R. R. Newman, R. C. Leedham, D. A. Purta, G. G. Madered and R. Galli, "Hot Bearing Detection with the SMART-BOLT," Proceedings of the 1990 ASME/IEEE Joint Railroad Conference, p. 105-10, 1990.

[13] Tarawneh, Constantine M., et al. "A Vibration Energy Approach Used to Identify Temperature Trending in Railroad Tapered-Roller Bearings." International Journal of Acoustics & Vibration 20.2 (2015).

[14] Wilson, Brent M., and Martin, Andrew. "Bearing Condition Monitoring Using Wireless Technology to Reduce the Risk of Bearing Failure." Proceedings of the ASME 2012 Rail Transportation Division Fall Technical Conference. ASME 2012 Rail Transportation Division Fall Technical Conference. Omaha, Nebraska, USA. October 16–18, 2012. pp. 213-222. ASME.

[15] J. A. Turner, B. M. Wilson, and L. Koester*. Service life testing of railroad bearings with known subsurface inclusions detected with advanced ultrasonic technology. Int. J. of Railway Technology, Vol. 2, No. 3, pp. 55-78, 2013.

[16] A. Gonzalez, "Development, Optimization, and Implementation of a Vibration Based Defect Detection Algorithm for Railroad Bearings," Master's Thesis, The University of Texas Rio Grande Valley, August 2015.

[17] Montalvo, J., "Defect Detection Algorithm Optimization for Use in Freight Railcar Service," Master's Thesis, The University of Texas Rio Grande Valley, August 2019.

[18] De Los Santos, N., Tarawneh, C., Jones, R., and Fuentes, A., “Defect Prognostic Models for Spall Growth in Railroad Bearing Rolling Elements,” Proceedings of the 2018 ASME Joint Rail Conference, Pittsburgh, PA, April 18-20, 2018.

[19] Jamison, W. E., J. J. Kauzlarich, and E. V. Mochel. "Geometric effects on the rib-roller contact in tapered roller bearings." AsLE Transactions 20.1 (1977): 79-88.

[20] C. Tarawneh, J. Lima, N. De Los Santos, and R. Jones. "Prognostics models for railroad tapered-roller bearings with spall defects on inner or outer rings," Tribology Transactions, accepted for publication, submitted February 2019.

[21] Slocum, A. H. (1992). Precision machine design. Englewood Cliffs, N.J: Prentice Hall.J.

[22] Montalvo, C. Tarawneh, J. Lima, J. Cuanang, and N. De Los Santos, “Estimating the outer ring defect size and remaining service life of freight railcar bearings using vibration signatures,” Proceedings of the 2019 ASME Joint Rail Conference, Snowbird, UT, April 9-12, 2019.

BIOGRAPHICAL SKETCH

Jennifer Danni Lima was born in San Juan, Texas. She is the youngest of three siblings. She went to Thomas Jefferson Early College Highschool. Later, she attended the University of Texas Pan American which became the University of Texas Rio Grande Valley, where she graduated Cum Laude with a Civil Engineering Degree. She earned her Master's in Mechanical Engineering in May 2020. Jennifer has accepted a job offer at Raytheon in McKinney, Texas. Jennifer can be contacted through her personal email jenniferdanni@live.com.